



HAL
open science

Enhanced mobility of iron and manganese on Mars: Evidence from kinetic experiments and models

Matteo Loche, Sébastien Fabre, Agnès Cousin, Arnaud Proietti, William Rapin, Benjamin Tutolo, Pierre-Yves Meslin, Anissa Benmammar, Foteine Dimitracopoulos, Roger Wiens, et al.

► To cite this version:

Matteo Loche, Sébastien Fabre, Agnès Cousin, Arnaud Proietti, William Rapin, et al.. Enhanced mobility of iron and manganese on Mars: Evidence from kinetic experiments and models. *Chemical Geology*, 2024, 662, pp.122242. 10.1016/j.chemgeo.2024.122242 . hal-04681811

HAL Id: hal-04681811

<https://hal.univ-reunion.fr/hal-04681811v1>

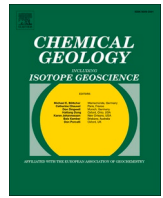
Submitted on 3 Sep 2024

HAL is a multi-disciplinary open access archive for the deposit and dissemination of scientific research documents, whether they are published or not. The documents may come from teaching and research institutions in France or abroad, or from public or private research centers.

L'archive ouverte pluridisciplinaire **HAL**, est destinée au dépôt et à la diffusion de documents scientifiques de niveau recherche, publiés ou non, émanant des établissements d'enseignement et de recherche français ou étrangers, des laboratoires publics ou privés.



Distributed under a Creative Commons Attribution 4.0 International License



Enhanced mobility of iron and manganese on Mars: Evidence from kinetic experiments and models

Matteo Loche^{a,*}, Sébastien Fabre^a, Agnès Cousin^a, Arnaud Proietti^b, William Rapin^a, Benjamin M. Tutolo^d, Pierre-Yves Meslin^a, Anissa Benmammar^c, Foteine Dimitracopoulos^e, Roger C. Wiens^f, Olivier Gasnault^a

^a Institut de Recherche en Astrophysique et Planétologie, Université Toulouse 3 Paul Sabatier, CNRS, CNES, 9 avenue du Colonel Roche, Toulouse 31400, France

^b Centre de microcaractérisation CASTAING, Université Toulouse 3 Paul Sabatier, Toulouse INP, INSA Toulouse, CNRS, Université de Toulouse, Espace Clément Ader, 3 Rue Caroline Aigle, Toulouse 31400, France

^c Université de La Réunion, Laboratoire GéoSciences Réunion, Saint-Denis 97744, France

^d Department of Earth, Energy, and Environment, University of Calgary, Calgary, AB T2N1N4, Canada

^e Institute of Meteoritics, University of New Mexico, NM, USA

^f Purdue University, West Lafayette, USA

ARTICLE INFO

Editor: Karen Johannesson

Keywords:

Mars
Weathering
Experiments
Models
Kinetics
Carbonates

ABSTRACT

Several missions have reported complex alteration mineralogies on early Mars, which preserve environmental records of multiple water-rock-atmosphere interactions. The MSL and M2020 missions in Gale and Jezero have identified Fe and Mn-bearing secondary phases. These elements are used as tracers for the redox conditions on both Earth and Mars. However, to fully understand the short-lived and local-scale processes observed on Mars, it is necessary to go beyond thermodynamic models and experiments. Enhancing our ability to interpret the redox and hydrological conditions from the observed phase assemblage requires understanding the evolution of Fe and Mn during weathering. This study reports the results of kinetic alteration experiments and geochemical models conducted under Mars-like conditions. We tested variable pO_2 , pCO_2 , temperatures, and starting solutions. The results suggest that Fe is more mobile on Mars than on Earth, with a pseudo-equilibrium concentration that is kinetically controlled by dissolution and oxidation rates. Despite some initially modeled siderite precipitation, no siderite precipitation was observed in the altered powder. Solutions with higher acid concentrations were primarily controlled by dissolution kinetics, with both Fe and Mn being mobile, even when a minor amount of P, Fe, and S bearing secondary phases are formed. Based on our experimental results, we updated the model and conducted two large-scale sensitivity tests on our kinetic simulation. We confirmed that our experiments were too high in pO_2 for siderite to form; however, we found that over a range of clearly oxidizing conditions from an equilibrium standpoint, Fe and Mn are mostly mobile, and siderite precipitation can occur. We were able to determine the pO_2 , pCO_2 and the temporal space where Fe-oxide or siderite predominate or coexist, constraining the meaning of reducing or oxidizing conditions. Moreover, we also observed that siderite formation would require a much longer water residence time than Fe-oxide to precipitate, interpreted as higher weathering rates, or later evaporation required to effectively precipitate under any conditions. On ancient Mars, both Fe and Mn would be relatively mobile and prone to be leached from their host rock. Observing siderite or oxide would not primarily be a redox marker but would be a clue to a different hydrological regime. At the planetary scale, it would be challenging to form authigenic siderite during alteration. Although siderite would not indicate the presence of a particularly reducing atmosphere and that Mn-oxides are mainly pH controlled and do not require terrestrial-level amounts of oxygen, a collocated precipitation of siderite and Mn-oxides could also provide valuable information to constrain the redox environment of the ancient Mars.

* Corresponding author.

E-mail address: matteo.loche@irap.omp.eu (M. Loche).

<https://doi.org/10.1016/j.chemgeo.2024.122242>

Received 27 March 2024; Received in revised form 15 June 2024; Accepted 19 June 2024

Available online 23 June 2024

0009-2541/© 2024 The Authors. Published by Elsevier B.V. This is an open access article under the CC BY license (<http://creativecommons.org/licenses/by/4.0/>).

1. Introduction

Episodic aqueous activity has been widely recorded within Mars' Noachian/Hesperian terrains, such as crater lakes or valley networks linked to alteration minerals identified from orbit (Ehlmann et al., 2008; Carter et al., 2013), as well as ancient lake and lake margin sediments at Gale and Jezero craters showing a wide diversity of secondary phases currently explored in situ (Grotzinger et al., 2014; Rampe et al., 2020b; Farley et al., 2022; Tice et al., 2022; Wiens et al., 2022; Mandon et al., 2023). The inventory of secondary phases showed complex hydrological systems with changing chemical, sedimentological and hydrological conditions. These secondary phases, namely clays, oxides, sulfates, carbonates, phosphates, chlorides and borates, were found in igneous and sedimentary rocks (lacustrine, fluvial, and subaeolian facies) and were sometimes overprinted by veins, diagenetic concretions, and were potentially cemented, advocating for a complex story involving different fluids and timing (Forni et al., 2015; Gasda et al., 2017; Rapin et al., 2019; Clavé et al., 2022). In particular, redox-sensitive elements such as Fe and Mn are found on Mars in several valence states, sometimes within the same sedimentary rocks. In Gale crater, several occurrences of minerals bearing different valence states of iron have been reported throughout the traverse: Nontronite, a clay that includes Fe^{2+} and Fe^{3+} , Fe and Mn oxides, as well as potential Fe / Mn phosphate (Rampe et al., 2020a; Lanza et al., 2016; Treiman et al., 2021). Recently, Fe-carbonates were detected in the Gale crater sulfate unit (Tutolo et al., 2024), as well as Fe–Mg carbonates in the Jezero crater (Clavé et al., 2022).

When primary silicate minerals are weathered, Fe^{2+} and Mn^{2+} are released in the alteration solution. Divalent Fe and Mn can form phases such as carbonates, sulfates, or phosphates and can also be integrated in some clays mixed with the trivalent state for Fe. The divalent state of Mn and Fe is mostly considered soluble, resulting in higher mobility when conditions do not permit the formation of divalent-bearing phases such as carbonates. The trivalent state (and higher valence state for Mn) is insoluble over a wide range of pH, and even at extremely low activities, will form oxides or oxyhydroxide. Oxidation of the divalent state of these elements requires oxidants: these oxidants can come from atmospheric O_2 or reduction of H_2O during alteration reactions, and can also result from photo-oxidation (Anbar and Holland, 1992; Oze and Sharma, 2007; Tabata, 2021). On Earth, Fe and Mn mineralogy in oceanic sediments can serve as a global marker for changes in atmospheric composition, such as the Great Oxidation Event that was proposed with the Banded Iron Formations (BIF) (Roscoe, 1973). On Mars, such global changes of the atmospheric composition have been posited on the basis of observations of oxides (Lanza et al., 2016). Planetary-scale terrestrial analogs have their limits: for example, the formation of BIF lasted for 100 s of My, in a continuously active hydrosphere and in an oceanic environmental context that differs from the short-lived lacustrine paleoenvironments explored on Mars (Konhauser et al., 2017). Moreover, these terrestrial deposits underwent pronounced diagenesis and metamorphism that are not comparable to those of Mars' conditions. In addition to planetary-scale changes, the different mineralogy of Fe and Mn can also highlight regional and local processes. Oxidation fronts in soils, lake beds and aquifers, bio-induced processes can result in the deposition of a variety of Fe and Mn minerals (Neugebauer et al., 2022; Limmer et al., 2023). Often overlooked, the kinetic processes of dissolution, oxidation, and precipitation are crucial for understanding the phase assemblage and the timings of events on a smaller scale. On Earth, many processes that are within the conditions where reactions are rate-dependent cannot be simply approached by equilibrium-only modeling (Steeffel et al., 2005; Steeffel, 2019). For instance, paleolaterite weathering profiles have been successfully modeled with kinetics and reactive transport (Myagkiy et al., 2019). On Mars, modeling and experimental studies have been carried out to explain regional or local deposition using kinetics and/or reactive transport (Zolotov and Mironenko, 2007; Bristow et al., 2017; Fairén et al., 2017; Hausrath et al., 2018; Viennet et al., 2019; Hausrath et al., 2021).

Most previous experimental works on the dissolution of silicates consisted of long-lasting experiments (up to several years), or/and increasing the temperature to enhance dissolution rates or/and increasing reactive surface and starting from a single type of silicate (Bullock et al., 2004; Dehouck et al., 2014a; Viennet et al., 2019; Baron et al., 2019; Gil-Lozano et al., 2024). However, this can induce some bias: for example, in dissolution experiments starting only with olivine, the lack of feldspar would mostly prevent clay formation because of the lack of Al in the solution, hence modifying both the fluid evolution and the final secondary phase assemblage by a negative feedback loop. This would limit the validity of the experiment extrapolation to natural cases, where dissolving rocks are, in fact, an intricate mixture of primary phases. The increase of temperature, despite its convenience, can inevitably alter the nature of the secondary phase assemblage and render results irrelevant for cold and arid early Mars environments. Some of these equilibrium-based “cook-and-look” experiments are often used to study hydrothermal alteration because a high temperature increases the rates to a point where the rates can be omitted. When looking at environmental conditions during the Noachian/Hesperian on Mars, particularly in the crater lakes explored by the Curiosity and Perseverance rovers, the hydrothermal approach might not be appropriate or sufficient to explain all the observations made, especially for surface weathering. Although conditions were favorable to the perennial existence of water, the climate might have been dry, cold, and rather short-lived on geological timescales during the Hesperian period (Stopar et al., 2006; Tosca and Knoll, 2009; Turbet and Forget, 2021; Wordsworth et al., 2021). These conditions of short-lived or reduced water-rock-atmosphere interactions mean that the alteration and oxidation reactions are more likely controlled by rate than by thermodynamic equilibrium. In such cases, the precipitation of redox-sensitive elements, such as Fe and Mn, could be controlled or inhibited by kinetic processes (Mitra et al., 2022; Loche et al., 2023). Even in a more favorable subsurface closed system, where the water-rock interaction persists for a longer period of time after the surface dries out, the temperatures and pressures could have been low enough for rate-limited alteration (Borlina et al., 2015). Some studies even propose that dissolution or precipitation kinetics could be the controlling factor at a global scale on Mars (Fairén et al., 2011; Bishop et al., 2018; Zolotov and Mironenko, 2007).

Our approach is focused on understanding the evolution of the fluid composition, specifically the fate of the redox-sensitive elements Mn and Fe. We are investigating the joint dissolution, oxidation, and precipitation of secondary phases through kinetic experiments. The kinetic aspect is key, providing new insights on dissolution, oxidation, and precipitation of secondary phases under Mars-relevant conditions. Our experimental approach consists of a systematic sensitivity test with several variations of parameters, using a precise description of the dissolving rock, the fluid evolution, and the secondary phase precipitation. In our approach, the starting material is a natural rock, the mineralogy of which is finely characterized for modeling purposes. We tested a new method to estimate the theoretical reactive surface area, as this data is not always available. There are multiple experimental conditions with variations in the mixture of atmospheric gases, the starting solution, and temperatures that reflect potential changes of Martian environmental conditions. We adapted our sampling strategy with a larger number of samples to obtain a better temporal resolution of the fluid evolution. We acknowledge that our short-lived (< 3 months) dissolution experiments will not be able to produce a large amount of altered material for some of the conditions we are testing. However, thanks to more advanced geochemical models, the objective is to help decipher the controlling parameters on the evolution of the concentration and eventually linking them to the secondary phase assemblage. From the experimental results and interpretation, we aim to adapt the model and to run large sensitivity tests that will help to unveil the paleoenvironmental and redox conditions controlling the precipitation of Fe and Mn-bearing phases at the surface of a once watery Mars.

2. Experimental approach and methods

2.1. Characterization and preparation of the starting material

The mineralogy of the starting material is guided by several aspects specific to the Martian approach. Since most of the Martian crust is of basaltic composition, and since the in-situ missions in ancient aqueous environments are observing basaltic-like precursor rock (Mangold et al., 2016; Farley et al., 2022), it is most likely that basalts were the major component of reacting materials on early Mars. The mineralogical phases of the basalts can be diverse: we have chosen to take a more mafic end-member of the basalts, with olivine in the phase assemblage. For a kinetic experiment, this is particularly important as olivine has the highest dissolution rate among the primary silicates, so it would be one of the highest contributors of ions to the weathering solution when in a rate-limited setting (Siever and Woodford, 1979). Olivine compositions also need to be Fe-rich, since Martian olivines tend to have a lower Mg content than their terrestrial counterparts. For example, olivine composition measured in-situ by the Curiosity rover with the CheMin

instrument are close to Fo(60) (Fo = Mg endmember of olivine, named Forsterite) (Koeppen and Hamilton, 2008; Rampe et al., 2020b) and between Fo(55) to Fo(73) in Jezero crater floor rocks (Wiens et al., 2022).

For logistical purposes, the mass required of the starting material is substantial due to the high number of experiments, as well as the increased volume of fluids to accommodate more sampling (Section 2.2). This increased amount of starting material would have been almost impossible to synthesize in a reasonable time, especially for several minerals - moreover, for minor elements such as Mn and P, the goal is to identify their natural abundance and distribution in phases; therefore, a natural basalt was selected as the starting material. Both natural rock or mineral and synthetic mineral assemblage have been used in previous experimental studies (Dehouck et al., 2014a; Gaudin et al., 2018). We required a sample with high crystallinity to avoid the presence of volcanic glasses - which would make the kinetic modeling more difficult - and that is as unaltered as possible to avoid any confusion due to pre-existing altered mineralogy. Using natural material gives more confidence in the extrapolations of results to natural cases. The

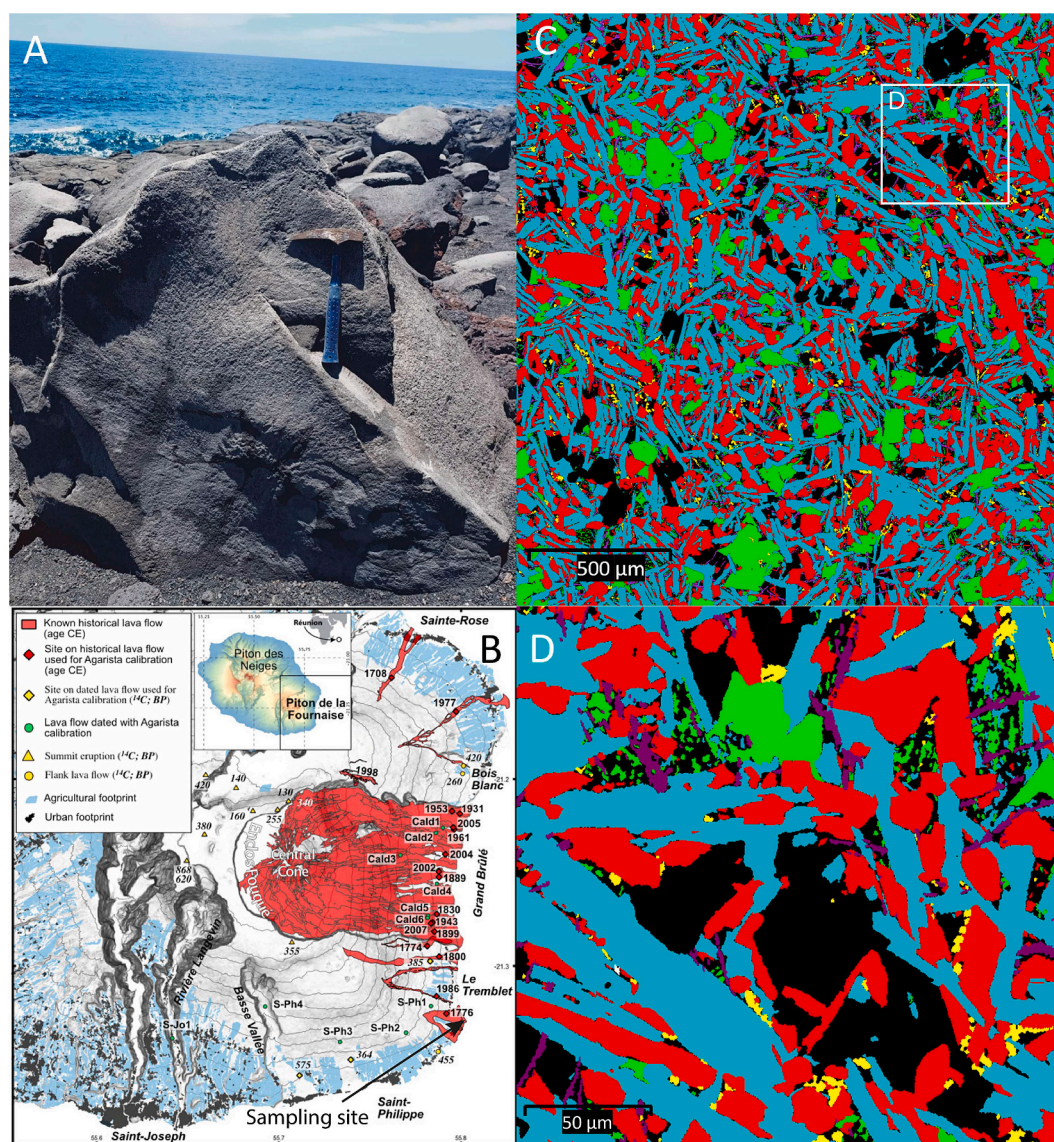


Fig. 1. (A) Sampling site at la Pointe du Tremblet. (B) Map of historical lava flows of the Piton de la Fournaise and localization of the sampling site (Albert et al., 2020). (C) EBSD map of sample one, with olivines in green, pyroxenes in red, feldspar in blue, ilmenite in yellow, titanomagnetite in purple and fluorapatite in white. Black color areas represent spaces without mineral identification and are categorized as porosity (D) Close up view of the EBSD scan, marked as a white box in (C). (For interpretation of the references to color in this figure legend, the reader is referred to the web version of this article.)

characterization method can also be reused more easily in a study focusing on a natural case with a known rock composition for in-situ studies on Mars or on Earth. For our experiment, we decided to test a single rock composition, aiming to keep the number of experiments reasonable (Section 2.2), but implementing in the model the option to process most of the other rock compositions (Section 3).

We sampled a basaltic lava flow from La Réunion Island in the Indian Ocean. The lava flow is located in the eastern part of the volcano, at the Pointe du Tremblet (Fig. 1). The basaltic lava flow was sampled in two spots where it was the most massive and pristine (localization: 21°19'51.58"S, 55°48'30.31"E and 21°19'51.27"S, 55°48'31.67"E). For rock characterization, we used a Field-Emission Scanning Electron Microscope (FEG-SEM), JEOL JSM 7100 TILS LV (Centre de Microcaractérisation Raimond Castaing, Université de Toulouse) equipped with a CMOS Electron BackScatter Diffraction (EBSD) camera (Symmetry S2, Oxford Instruments) coupled with a Energy Dispersive Spectroscopy (EDS) detector (Ultim Max 100 mm², Oxford Instruments). From the pristine rock batch, we extracted two samples for analysis (87-1 and 87-2). Two large EDS/EBSD mappings (1.65 × 1.65 mm) were performed on each sample at accelerating voltage of 20 kV, a working distance of 15 mm and a step size of 0.5 μm in order to determine grain morphology, mineral distribution, and phase proportion. Once the minerals were identified, porous area was also quantified to normalize the proportion of surface area per phase. The proportion of the surface areas was then converted to volumetric surface areas using a spherical assumption (Table 1). The proportion of K-feldspar could not be determined using XRD as they could not be identified by the solver, but it was detected and confirmed using the EDS data. To determine their global volumetric proportion, we used another method in which we first estimated the total mineral occurrences ($n = 49$) in the same 0.24 mm² area and then determined their average surface area using an ellipse assumption on a few minerals ($n = 3$), since their sizes were homogeneous throughout the section. The global proportion was then estimated by looking at the total specific surface of K-feldspar relative to the considered surface area.

For modeling purposes, it is important to have good knowledge of the mineral assemblage, including the most accurate solid solution compositions of the most abundant rock constituent minerals. Moreover, we want to know the quantity and distribution of less abundant elements such as P and Mn, and the nature of the phases that include them. Using EDS elemental maps, we assessed potential mineral zoning by looking at the spatial variation of composition within individual crystals; olivines were more heavily zoned with Fe-rich edges and Mg-rich cores. All olivine grains in two 0.24 mm² areas (enough to have at least a dozen of each mineral) of each sample (87-1 and 87-2) were sampled in their minor and major axes with EDS profiles (1 μm step-size), assuming an ellipsoid geometry. Using Eq. (1), we calculated the atomic fraction F of each component of the solid solution in the solid solution for one mineral, with \overline{F}_{min} and \overline{F}_{max} being the average atomic fraction over the minor and major axis of the assumed ellipse, L_{min} and L_{max} being the length in μm of axes and L_T their sum.

Table 1

Mineral phase compositions and proportions extracted from EBSD and EDS data. Proportion of manganese in the solid solution. Surface area proportions are converted to volumetric proportions assuming spherical geometry.

Mineral Phase	Solid Solution	Mn (%)	Volumetric Proportion (%)
Olivine	Fo(75), Fa(25)	0.52	5.74
Pyroxene	En(41), Wo(43), Fs(16)	0.55	28.11
Plagioclase	Ab(35), An(65)	–	64.88
K-feldspar	Ab(63), Mc(37)	–	0.57
Ilmenite	–	–	0.96
Titanomagnetite	–	–	0.23
Fluorapatite	–	–	0.002

$$\overline{F} = \frac{L_{min}}{L_T} \overline{F}_{min} + \frac{L_{max}}{L_T} \overline{F}_{max} \quad (1)$$

Using Eq. (2), we estimated the global atomic fraction F_{at} for the considered area. Individual mineral volume V is calculated using an ellipsoid geometry approximation considering that the lengths of the minor axes are equal in y and z dimensions and summed to find V_T . The final fraction F_{at} of each sample is then averaged to give the final solid solution composition.

$$F_{at} = \sum_{i=1}^n \overline{F}_i \frac{V_i}{V_T} \quad (2)$$

This methodology was applied on olivines ($n = 17$), pyroxenes ($n = 12$) and plagioclases ($n = 8$). The size and composition variations of pyroxene and plagioclase feldspar were not as high as those of olivine, so the measurement was not systematic within the same area. The general composition of K-feldspar solid solutions was calculated by averaging their composition of solid solutions measured with EDS points ($n = 52$) independently of their geometry. For the other minor phases, inspections were carried out to identify their phase; F in P-bearing phases indicated that it was fluorapatite and different Ti/Fe ratios confirmed the presence of titanomagnetite and ilmenite ($n = 19$).

To prepare the starting material for the experiment, the rock fragments from la Reunion island were systematically cut using a circular saw with diamond blade to remove exposed edges and keep the most pristine unaltered core. The prepared samples were then processed in a rock grinder to obtain a powder. Powders were then sieved to obtain a grain size fraction of 100–200 μm and cleaned with ultra-sound in a bath of ethanol to remove any remaining finer particles. The process was repeated until the ethanol remained clear of particles. The 100–200 μm grain size fraction was chosen because it is close to what could have been the reactive surface of Martian glacial collovium, speeding up slightly the reaction compared to coarser sediments but remaining a valid analog (see references and details in Section 6.1). Finally, the powder was placed in a oven at 110 °C for 12 h to be sterilized. The process was repeated twice to collect enough material to run all the experiments - a total of 600 g, with 50 g per reactor.

2.2. Experimental setup

The experimental setup was designed to allow a fast, secure, and easy fluid sampling, as well as efficient atmospheric control. It is essentially composed of three parts: the reactors, the Fluid Management Devices (FMD), and the sample container. The FMD and the sample container are composed of Swagelok™ 316 Stainless Steel plumbing while the reactors are composed of a DURAN™ borosilicate bottle, comprising a GLS80 cap with four GL18 connectors. Two connectors are closed, and two other connectors are linked to the gas and fluid management device by 1/8" PFA transparent tubes. One tube is plunged into the fluid and the other is connected to the reactor atmosphere. Each end of the tubes is connected to the fluid management device using Swagelok™ 1/4" double flow, double sealed, quick connect system. The fluid management device is equipped with one gas inlet, one gas outlet, two quick connects for connecting the reactor and one quick connect for the sampling container (Fig. 2). A manometer is also connected to monitor the pressure. Each reactor has its own fluid management device, with its gas inlet connected to a gas distribution tube connected to the O₂ and CO₂ bottle. To adjust the gas mixture between O₂ and CO₂, a Pyro™ FDO₂ digital oxygen meter with a custom 3D printed flow trough cell can be connected to the gas flush outlet of the devices. The sample container has a quick connect stem that mates with the quick connect on the fluid management device, while the other end has a quick connect body. In between, the fluid is stored in a larger 1/2" clear PFA tubing, allowing visual control of the fluid level for a total volume of 15 ml. To draw fluid from the reactor into the sample container, the quick connect end can be

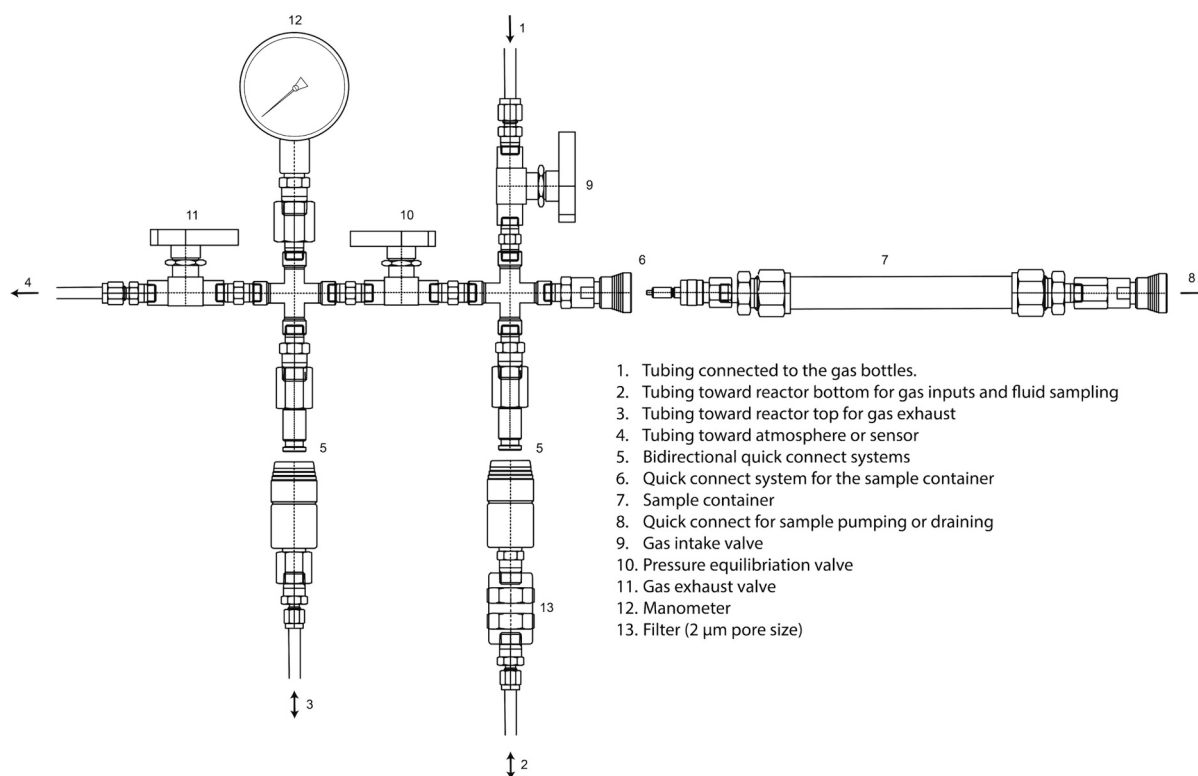


Fig. 2. Scheme of the Fluid Management Device (FMD) and of the sample container. Each reactor is connected to one device so experiments can be isolated from each others to avoid contaminations.

connected to a vacuum vessel with a valve to control the flow. To remove fluid from the container, two single quick connectors can be connected at either end.

The experiment overall consists of 12 reactors and 4 blanks, summarized in Fig. 3 and Table 2. Among the reactors, 8 are under controlled atmosphere and 4 are witnesses under terrestrial atmosphere (W = terrestrial witnesses, or control). For the starting solution, 6 reactors start with pure water and 6 start with an acid solution (α = Acid starting solution). The acids' concentrations for this solution are $\text{H}_2\text{SO}_4 = 6.77 \times 10^{-2} \text{ mol l}^{-1}$ and $\text{HCl} = 1.94 \times 10^{-2} \text{ mol l}^{-1}$ (Fig. 3). This is based on the in-situ measurement made by APXS on Curiosity rover on the Rocknest target (Blake et al., 2013). This particular target might represent a relatively unaltered composition of the source rock, and has

been previously used as a proxy for initial composition for Gale crater (Tosca et al., 2018). The acid concentration is based on the S/Cl ratios and abundances measured in this target, and we use these as a proxy for the highest concentration of acid that could be present in an hypothetical Martian surface starting solution. Among the 12 reactors, 6 reactors are in an oven at 60°C (H = Higher temperature 60°C "Hot") and 6 are at ambient temperature (A = Ambient temperature 23°C average), and both with temperature monitored. Placing the reactor directly in an oven avoids temperature gradients, as reported in some previous experiments using a heating plate (Dehouck et al., 2014b). For the 8 reactors under controlled atmosphere, 4 contain an atmospheric mixture of 10% O_2 / 90% CO_2 (O_2^+) while the remaining 4 contain a mixture of 1% O_2 / 99% CO_2 (O_2^-). (Fig. 3). The maximum value of 10% O_2 was chosen as the

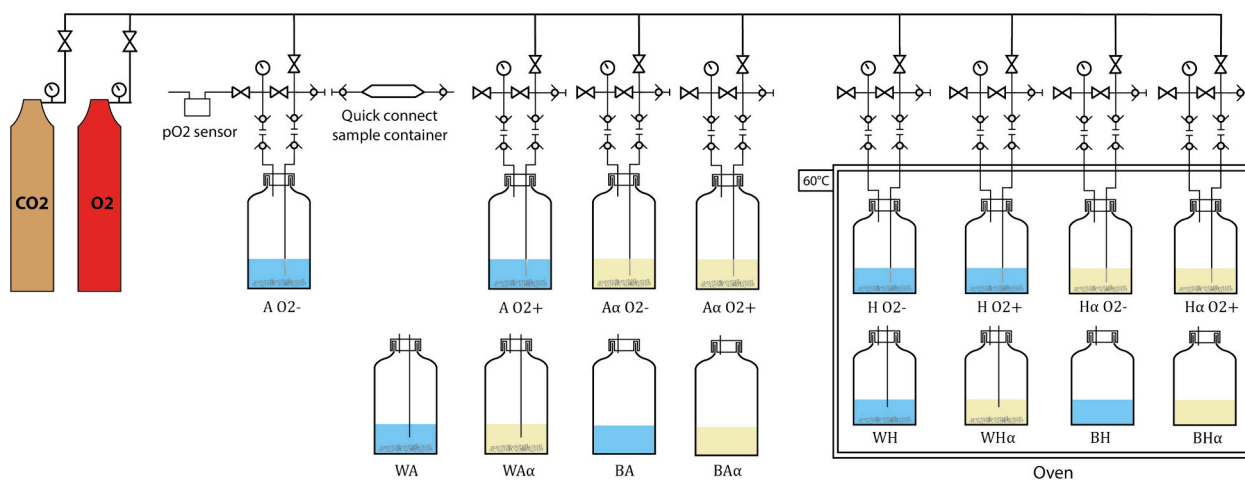


Fig. 3. Scheme of the experimental setup. Experiment names are constructed according to the combination of experimental conditions: A = Ambient temperature (23°C average), H = Higher temperature 60°C ("Hot"), W = terrestrial witnesses, α = Acid starting solution, O_2^- = 1% O_2 /99% CO_2 , O_2^+ = 10% O_2 /90% CO_2 .

Table 2
Summary of experimental conditions.

Experiment	Temperature	Initial solution	O ₂ (%)	CO ₂ (%)
AO ₂ ⁻	Ambient (23 °C)	Pure water	1	99
AO ₂ ⁺	Ambient (23 °C)	Pure water	10	90
WA	Ambient (23 °C)	Pure water	Terrestrial	Terrestrial
HO ₂ ⁻	High (60 °C)	Pure water	1	99
HO ₂ ⁺	High (60 °C)	Pure water	10	90
WH	High (60 °C)	Pure water	Terrestrial	Terrestrial
AαO ₂ ⁻	Ambient (23 °C)	Acid solution	1	99
AαO ₂ ⁺	Ambient (23 °C)	Acid solution	10	90
WAα	Ambient (23 °C)	Acid solution	Terrestrial	Terrestrial
HαO ₂ ⁻	High (60 °C)	Acid solution	1	99
HαO ₂ ⁺	High (60 °C)	Acid solution	10	90
WHα	High (60 °C)	Acid solution	Terrestrial	Terrestrial

maximum episodic value reached in Mars atmospheric modeling that results from episodic warming (Wordsworth et al., 2021). It provides one possible upper limit that favors faster oxidation rates within the scope of the experiments. As the goal of the experiment is to decipher the difference in rates due to a change in pO₂, we preferred to have a second batch of experiments at lower pO₂ than under pure CO₂, based one order of magnitude lower than the maximum value. To correct for any contamination from the reactor, 4 blanks are performed in a terrestrial atmosphere, with 2 starting with pure water and 2 others with the acids solution, and 2 at ambient temperature and 2 at 60° without the starting material.

At higher temperatures, we expected the dissolution reactions to be faster, so the experiments were set for a duration of 14 days. Experiments at ambient temperatures were expected to have lower dissolution rates, so their duration was set at 80 days. This is rather short compared to other experiments that aimed to observe larger changes in the mineral mixture, which can last for 6 months up to several years (Bullock et al., 2004; Dehouck et al., 2012, 2016; Gaudin et al., 2018; Baron et al., 2019). Other similar experiments were performed with a shorter duration, but changes were still observed in the mineral mixture and in the solution (Dehouck et al., 2014a). Because of our kinetic approach and the initial conditions far from equilibrium, most of the dissolution will occur in the short term; this was the motivation behind the choice for a shorter experiment runtime.

2.3. Reactors preparation

Before starting the experiments, all reactors and their plumbing are sterilized in an oven at 110 °C for 12 h. 500 ml of starting solution is prepared using MilliQTM ultrapure water and weighed for each run to achieve W/R = 10 (Water/Rock ratio, in mass). When the initial preparations are complete, the reactors and their caps/connectors and starting solutions are transferred to an anoxic glove box to be degassed 24 h before the start of the experiment. Inside the glove box, the rock powder is weighed and 50 g is transferred into each reactor; then the starting solutions are added and the reactor is sealed. Batch 1 (B1) was used for witness and O₂⁻ experiments, and batch 2 (B2) was used for O₂⁺ experiments.

Immediately after sealing, the reactors are quickly transferred outside, placed on the bench or in the oven depending on their operating temperature, connected to the fluid management device and flushed several times with CO₂. To achieve the desired O₂ content for each run, we create a pure O₂ flow by opening the inlet and outlet valves and maintaining a pressure of 1.2 bar by adjusting the valve opening, while the partial pressure of oxygen is monitored by the O₂ sensor placed on the exhaust line. During operation, the gas content is periodically adjusted to maintain the pressure and composition of the gas mixture. In addition, the reactors are gently stirred by hand every day.

2.4. Sampling

To acquire a sample, the sample container is connected to the fluid management device and the fluid sample is pumped out of the reactor (Section 2.2). The fluid container is immediately transferred inside the glovebox for analysis under anoxic conditions. Inside the glove-box, 5 ml of the raw fluid sample is placed in a small-diameter glass container, and a pH probe (VWR pH 100TM) is inserted into it. The pH record is taken for a few minutes when a value is stabilized. For fluid samples at 60 °C, the measurement is initiated when the sample is cooled to room temperature after a few minutes. To measure the dissolved O₂, we use a PME miniDOTTM sensor. We completely cover the O₂ sensor with 1 to 3 ml of raw solution for 3 min and record the dissolved O₂ value before the fluid has an opportunity to degas significantly. For later analysis, around 5 ml of fluid is filtered using a 0.2 μm disk filter and stored in PFA SavilleTM vials for later concentration analysis.

In total, sampling of the fluid from the reactors is performed 10 times using the fluid management device, and for the final sampling, directly in the reactor using a pipette within the glovebox. For witness experiments, the fluid is sampled directly using a pipette 11 times. For the 80 days experiments ("A" Ambient temperature runs), the fluid is sampled at 24 h, 96 h, 8 days, 14 days, 20 days and then each 10 days until the final sample. For the 14 days experiments ("H" High/Hot temperature runs), fluid was sampled every 24 h until day 9 and then every two days until the final sampling. The sampling frequency decreases over time to allow a better temporal resolution of the fluid composition when the dissolution rates are higher at the beginning of each experiment. Each sample contains 15 ml of solution, which is equivalent to approximately a 30% reduction of W/R at the end of the experiments. This value is higher than the 10% of shift that is common in other comparable studies. The reduction of W/R will reduce the time required to reach a given concentration, hence reducing the time required to reach saturation of the secondary phases. The feedback effect of increased ions' activities will also cause a decrease in dissolution rates, buffering the initial effect. As we are performing experiments that are far from equilibrium, the effect of lowering W/R should be negligible in these timescales. It is assumed that a value of 30% is considered acceptable, and the advantage of having a larger number of samples is seen as more important than the potential risk of encountering limited rate discrepancies due to a change in W/R.

At the end of each experiment, the reactors are disconnected from the fluid management device and transferred inside the glovebox. A final 11th sample is taken using a pipette and goes through the same process as the previous samples. The fluid is then poured into the reactor through a chemical filter to collect any fine particles of secondary phases. If any phases are visually observable in the filters, they are kept and dried on paper. The altered rock powder at the bottom of the reactor is then collected and quickly placed to dry between absorbing paper sheets for a day, and then sealed in a plastic container for later analysis.

2.5. Fluid analysis

Stored fluids samples are analyzed at the end of the experiments to obtain concentrations of the major elements including Si, Al, Fe, Mn, Mg, Ca, Na, K, Ti and P. Fluid samples were all analyzed with an ICP-OES iCap6500 by the SARM (Service d'Analyse des Roches et des Minéraux) of the CRPG in Nancy, France. The uncertainties in the measured concentrations were provided by the SARM and are based on georeference materials (river water and drinking water references, Yeghicheyan et al. (2019, 2021)). They can be found in the supplementary material appendix C. In addition to the experimental samples, fluid samples from the 4 blank runs were sent to SARM, as well as 2 blank samples for filters. All data presented in the results were adjusted with the corresponding blank experiment values and from the filters values.

2.6. Solids analysis

While the study focuses on the alteration fluids, the investigation of the produced secondary phase assemblage can give complementary informations. We analyzed a total of 12 altered rock powders from the 8 runs under “Martian” (CO₂) atmospheric conditions and 4 from the witness runs (Table 2). Additionally, we analyzed 4 samples from the 4 final fluid filtration that contained enough material to be collected. From the knowledge of previous experiments and because of the short duration of our experiments, we anticipated that the amount of secondary phases will be extremely reduced, especially for the runs without the acidic starting solutions. For this reason, we analyzed all samples using a FEG-SEM (JEOL JSM 7800F prime) coupled with an EDS detector (X-Max 80mm², Oxford Instruments) at the Centre de Microcaractérisation Raimond Castaing, Toulouse, France. This technique allows closer inspections of mineral surfaces to make a qualitative analysis of the phase assemblage and, when possible, identification of secondary phases using stoichiometry with the chemistry data acquired with the EDS. Although this technique is not directly sensitive to mineralogy and cannot be used to estimate the bulk phase assemblage, conventional powder XRD would give mixed results on the least altered powders with a sparse amount of secondary phases. Mineral grains were investigated by looking at dissolution patterns and secondary phase patterns at the surface of the grains. EDS elemental maps as well as EDS points and profiles were used to investigate the chemical signature of secondary phases and determine their stoichiometry when possible. Although Oxford Instruments does not provide uncertainties on quantification, the limit of quantification of EDS is 0.1% (atomic percent) on this instrument.

3. Geochemical modeling

3.1. Modeling software and database

The simulations were conducted with PHREEQC 3.7, which was developed by the USGS. PHREEQC is a batch reaction code capable of computing a variety of calculations such as speciation, equilibrium between solids, aqueous solutions and gases or kinetic rate laws. Thermodynamic properties of minerals, gases, and dissolved species are stored in a database and used to compute equilibrium calculations and saturation indices over a wide range of pressures and temperatures (Parkhurst and Appelo, 2013). For this model, we used the Thermoddem database from the French geological survey, Bureau des Recherches Géologiques et Minières (BRGM). This database contains hundreds of phases, is self-consistent and is often updated (Blanc et al., 2012). In addition to Thermoddem, we added the estimated parameters for jahnsite-whitcheite, a Mn-phosphate, and corrections for the phases Vivianite, CaAlH(PO₄)₂·6H₂O and MgHPO₄ (Drouet et al., 2021). To be able to model oxidation rates and dissolution/precipitation of phases including Fe and Mn, we modified every solid or aqueous species in the database to be handled by PHREEQC, adding the Fe(II)/Fe(III) and Mn (II)/Mn(III) distinctions in the dissolution equations. Also, to better model Fe and Mn dissolved species, we completed the database with solid phases and solutions species which were critically lacking for these elements. The detailed explanations about the modification of the database and the tables listing the phases and their thermodynamic properties can be found in the supplementary material appendix A. For calculation of sensitivity tests (Sections 6.2 and 6.3), we used Python with the PhreeqPy software (Müller et al., 2011) to run our kinetic simulation on parallelized IPhreeqc COM servers (Charlton and Parkhurst, 2011) and extract data cubes.

3.2. Data and modeling of the rock powder dissolution

Modeling of the starting solid is important as it is one of the main controlling factors. The volumetric fraction and the composition of the

solid solutions for each major phase were determined using EDS and EBSD (Section 2.1). As the rocks are crushed to powder with a grain size mainly equivalent to or smaller than the mineral grain size (100–200 μm), we considered that the composition of the exposed surface of the minerals in the grains is equivalent to the estimated solid solution. To bring flexibility for the description of a starting rock in a kinetic dissolution model, we developed a Python Thermo-Kinetic calculator for PHREEQC. This calculator takes input from a parameter table with temperature, total mass of powder, and maximum/minimum grain diameter to estimate geometric reactive surface areas. A second input table allows the user to describe the rock composition: for each mineral, the user can describe a solid solution by balancing end-members, and describing the relative volumetric proportion of the mineral in the rock. The output is a text file containing lines of code that can be used directly in PHREEQC: 1- The *Phases* function of PHREEQC with the corresponding balanced equation of dissolution and log K at given temperature for each phase. 2- The *Kinetics* function of PHREEQC with all corresponding kinetic parameters including reactive surfaces and the initial molar quantity for each phase. For the calculations, the code gathers data for the thermodynamic temperature dependency and the kinetics rates constants in two databases which can be edited by the user. For now, the minerals available for calculations are olivine, pyroxene (3 end-members, augite type), orthopyroxene (2 end-members), clinopyroxene (2 end-members), plagioclase, K-feldspar, quartz, magnetite, fluorapatite, hydroxyapatite, muscovite, annite, ilmenite, glaucophane, riebeckite, and pyrite. Pyroxene and olivine do include the option to add an additional Mn end-member in their solid solution, assuming a congruent dissolution of Mn following the custom phase rate law.

For each solid solution, we calculate the individual log K at a given temperature using a polynomial fit function (Eq. (3)), where *A*, *B*, *C*, *D*, *E* are fit constants (all listed online on the Thermoddem database (Blanc et al., 2012)), *T* is the temperature in Kelvin.

$$\log_{10} K(T) = A + B \cdot T + C \cdot T^{-1} + D \cdot \log_{10}(T) + E \cdot T^{-2}(T) \quad (3)$$

Once the individual end-member log K is found, the custom log K for solid solutions K_{ss} are calculated using Raoult's law (Eq. (4)) where F_i is the fraction of the considered endmember in the solid solution, ΔG_i is the Gibbs free energy, *R* is the Gas Constant and *T* is the temperature in Kelvin.

$$K_{ss}(T) = \exp \left\{ - \left(\sum_i \frac{F_i \Delta G_i^0}{RT} + \sum_i F_i \ln F_i \right) \right\} \quad (4)$$

For the kinetics of dissolution, we use expressions derived from the Transition State Theory (Lasaga, 1981). Eq. (5) is a synthesis of the two main kinetics rate parameters compilations in the literature (Palandri and Kharaka, 2004; Heřmanská et al., 2022). The equations describe 3 mechanisms for acid, neutral and basic pH domains (depending on data availability) to describe the rate dm/dt in mol·s⁻¹ at a temperature *T* in Kelvin. With *SA* as the reactive surface area in m², for each mechanism $k_{\text{mechanism}}^{298.15K}$ the rate constant at 298.15 K, *E* is the activation energy in J·s⁻¹, *R* is the Gas Constant, Ω is the mineral saturation index which is equal to activity product divided by the equilibrium constant and σ , the Temkin's average stoichiometric Si number in the considered mineral. The dimensionless term $a_{H^+}^{\pm}$ is a function of the activity of the proton and raised to *n* the reaction order, which is negative for the basic mechanism. Regarding the kinetic dissolution of the K-feldspar, the aluminum inhibition is implemented by dividing a_{H^+} with $a_{Al^{3+}}$ in its rate equation (Oelkers et al., 1994). Calculation of the kinetics parameters *k* and *n* for a solid solution are performed by the thermo-kinetic calculator by calculating the arithmetic mean of the end-member parameters ponderated by the end-member fraction in the solid solution F_{at} .

$$\frac{dm}{dt} = -SA \begin{bmatrix} k_{\text{acid}}^{298.15K} e^{-\frac{E_{\text{acid}}}{R} \left(\frac{1}{T} - \frac{1}{298.15K} \right)} a_{H^+}^{n_1} \\ + k_{\text{neutral}}^{298.15K} e^{-\frac{E_{\text{neutral}}}{R} \left(\frac{1}{T} - \frac{1}{298.15K} \right)} \\ + k_{\text{base}}^{298.15K} e^{-\frac{E_{\text{base}}}{R} \left(\frac{1}{T} - \frac{1}{298.15K} \right)} a_{H^+}^{n_3} \end{bmatrix} (1 - \Omega^\sigma) \quad (5)$$

The total reactive area SA can be estimated using the Tester approximation equation assuming a normal distribution of grains. 6 (Tester et al., 1994) with F_{mi} as the mineral mass fraction, M_T as the total mass of the starting material, D_{max} and D_{min} as the maximum and minimum grain size diameter and ρ_i as the density of the specific mineral. In our calculations, mineral specific surface areas were used. In the model, the evolution of SA as the dissolution progresses is modeled with a spherical core shrink approach, with M_0 as the starting moles estimated using initial F_{mi} and M_T updated at each time increment with the molar quantity left for each considered phases.

$$SA = \sum_{i=1}^n \left(\frac{F_{mi} M_T}{M_0} \right)^{\frac{2}{3}} M_T \frac{6}{(D_{\text{max}} - D_{\text{min}}) \left(\ln \left(\frac{D_{\text{max}}}{D_{\text{min}}} \right) \right)} \cdot \rho_i \quad (6)$$

To be compared with our geometrical method of estimation, the total surface areas were measured for the two batches of rock powder (B1 and B2) using the Brunauer–Emmett–Teller (BET) technique at CIRIMAT, Toulouse, France, using krypton gas with the Micromeritics ASAP 2010 instrument. SA values are respectively $0.1831 \pm 0.0026 \text{ m}^2 \cdot \text{g}^{-1}$ and $0.1818 \pm 0.0021 \text{ m}^2 \cdot \text{g}^{-1}$.

To have more comparison points for interpretation of the results, we also performed equilibrium-based calculations. Using the “equilibrium” function of PHREEQC, we placed the calculated phase assemblage in equilibrium with the corresponding atmosphere and starting solutions. The final concentration was then compared to the last experimental data point in each experiment (Table 5, “equi1”). Additionally, with the method described in the Section 3.4, we also made a model in which both the primary minerals and secondary minerals are in equilibrium with the starting solution and gas mixture (Table 5, “equi 1 + 2”).

3.3. Modeling of the oxidation kinetics

Modeling of the oxidation kinetics of aqueous species is a critical part of the model to understand the evolution of the concentration. Both Fe (III) and Mn(III) are thermodynamically stable even at extremely low pO_2 , so the main control on their concentration, and hence on their mobility and on the secondary phase assemblage, will be the kinetics of oxidation. On Earth, Fe and Mn are rapidly oxidized due to higher pH and higher oxygen content in the atmosphere. In natural waters at pH 8, the typical half-life of Fe is only a few minutes while for Mn it is about 29 days (Sigg et al., 2022). Another determining factor is the bacterial catalysis, which can increase its oxidation rates by at least an order of magnitude (Morgan, 2005). On Mars, due to the absence of bacterial catalysis and the lack of a photosynthetic-driven mechanism that raises the pH of natural waters above 9, along with a decrease in surface water pH caused by higher pCO_2 and lower pO_2 , it is probable that the behavior of both Fe and Mn is primarily controlled by their oxidation kinetics. It is acknowledged in the literature that Mn-oxides could be challenging to form in these conditions without having alternative oxidants (Mittra et al., 2022). Previous Mars models considered the oxidation kinetics of Fe within a kinetic alteration model (Zolotov and Mironenko, 2007). Unlike previous models, our model combines both Mn and Fe oxidation kinetics while computing phase dissolution and precipitation. We acknowledge that a complete understanding of Fe and Mn abiotic oxidation can be more challenging, because they can both be catalyzed by metal oxide surfaces including self catalysis (Martin, 2005; Lan et al., 2017).

The rate law for Fe oxidation is a well described and understood process that was proved in the field (Eq. (7)) (Singer and Stumm, 1970). In this equation, the concentration decrease of $[Fe^{2+}]$ and the stoichiometric increase of $[Fe^{3+}]$ in $\text{mol} \cdot \text{s}^{-1}$ is described by two mechanisms. For pH above 3.5, the rate is described with the product of k , the rate constant of oxidation multiplied by the oxygen concentration $[O_2]$, the activity of iron II $[Fe^{2+}]$ and the pH with the activity of $[OH^-]$ raised to the power of 2 (Eq. (7)). This means that each pH unit will result in a change of the oxidation rate by a factor 100. The other mechanism valid under pH 3.5 describes that at low pH, control on the oxidation rate is no longer pH dependent, with only k' , $[O_2]$ and $[Fe^{2+}]$.

$$-\frac{d[Fe^{2+}]}{dt} = \frac{d[Fe^{3+}]}{dt} = k[Fe^{2+}][O_2][OH^-]^2 + k'[Fe^{2+}][O_2] \quad (7)$$

Similarly to the Fe oxidation rate, the Mn oxidation rate law is controlled mainly by pH. On the other hand, unlike Fe, the rate of oxidation is orders of magnitude lower. On Earth, oxidation of Mn especially occurs mainly at pH above 9, and is also catalyzed by bacterial activity. The description of the decrease of $[Mn^{2+}]$ in $\text{mol} \cdot \text{s}^{-1}$ is described by Eq. (8). This equation involves three kinetics rate constants k_1 , k_2 and k_3 to better describe the Mn speciation. These 3 species reactions and log K were added to the database with the same parameters reported in (Morgan, 2005). Oxidation of Mn is a complex process involving several steps, but speciation is poorly described in thermodynamic databases. As a result, we hypothesized that each removed moles of $[Mn^{2+}]$ will result in the addition of the same molar amount of $[Mn^{3+}]$. Having only $[Mn^{3+}]$ as higher valence state (oxidized) Mn ions is consistent with the database, which does not provide other secondary phases that form with other higher valence states.

$$\begin{aligned} -\frac{d[Mn^{2+}]}{dt} &= \frac{d[Mn^{3+}]}{dt} \\ &= -4[O_2] \left(k_1[MnOH^+] + k_2[Mn(OH)_2(aq)] + k_3[Mn(CO_3)_2^{2-}] \right) \end{aligned} \quad (8)$$

We have to note that both Mn and Fe rate laws are restricted to 25 °C and do not include temperature dependencies. It is reasonable to assume that in the scope of this work, the modification in oxidation speed should be limited, but that for even higher or lower temperatures, oxidation speeds might be affected.

3.4. Modeling of the precipitation of the secondary phases

Evolution of the fluid composition can be controlled or partially controlled by precipitation of secondary phases, when their precipitation causes a decrease in the concentration of some dissolved species. This control can be purely thermodynamic (depending on phase solubility) but can also depend on the considered mineral precipitation rate. Precipitation rates vary by several orders of magnitude depending on the secondary phases considered: clays are notably much slower to precipitate than other phases such as sulfates or oxides, which can have implications for phases assemblages found on Mars (Fairén et al., 2011). We can model secondary phase precipitation using two different approaches: thermodynamic precipitation or kinetic precipitation. Modeling of the kinetic precipitation can induce some bias, as few precipitation kinetic rate constants are available in comparison to dissolution rate constants, limiting the pool of possible phases (Marty et al., 2015). Alternatively, an easier way to integrate a greater number of precipitation kinetics is to consider the principle of micro-reversibility (Lasaga, 1998). However, precipitation remains a modeling challenge, as some parameters and mechanisms such as precipitation surfaces, nucleation sites or crystal growth are difficult to estimate.

In this study, we therefore focused on a thermodynamic approach: we began by narrowing down the number of potential secondary phases

that can precipitate by running a scan model with dissolution only, and determined the phases which reached saturation at any step in the model. Starting from this list of phases, we considered that when a phase saturation index will be above 1, it will start to precipitate. This approach allows for the computation of many secondary phases due to the large number of known log K in the literature. The downside of this approach is that it neglects the kinetic aspect of precipitation, which can significantly alter the result when the rate laws of certain phases are extremely slow, such as clays. It will also favor phases with low solubility, such as in the case of iron oxides, where hematite will always precipitate instead of goethite. This can negatively impact the predicted phase assemblage as low solubility phases will quickly scavenge most of the available ions and prevent the formation of other potential phases. To diminish this negative effect, we removed phases which were considered unrealistic to precipitate in the experiment, but can still reach saturation in the simulation because of high ion activities (such as quartz for Si phases). The complete list of initial phases can be found in the supplementary material appendix A.

4. Experimental results

The molar concentrations for total dissolved Mn and Fe over time are shown in Fig. 4. Each plot is arranged in a grid depending on the experimental conditions (starting solution, temperature and gas mixture). The complete dataset with all 10 elements is available in the supplementary material appendix C.

4.1. Analysis of the fluid composition evolution

Looking first at the experiments carried out at room temperature (23 °C) for 3 months and starting with pure water, we notice that the overall Fe concentrations are more important in the Mars-like reactors than in the witness reactors with 2 to 5 times larger for Fe and 5 to 15 times larger for Mn. However, concentrations in the AO_2^- run have around 3 times higher Fe and 10 times higher concentration of Mn than the one in AO_2^+ . For AO_2^- , the trends of Fe and Mn are correlated and show a rapid increase in concentration forming a peak around 4 days after the start and rapid decrease after 8 days, reaching a low and stable concentration around 14 days. For AO_2^+ Fe and Mn do not correlate for the peak. The concentration of Fe follows a similar trend that in AO_2^- with a concentration peak reached after only 24 h, a decrease and a second lower peak at 14 days and a decrease and a stable trend after 40 days. On the other hand, its Mn concentration also has a sharp increase after only 24 h but stays at this higher concentration for the rest of the experiments, while being 10 times lower in absolute value than the AO_2^- peak concentration. However, the concentration of Mn in AO_2^- is close to the AO_2^+ concentration after the peak. For the witness under terrestrial atmosphere WA, Mn and Fe are mostly correlated and below the limit of detection for the first 40 days, and a peak occurs around 60 days before decreasing at the end of the experiment.

For experiments with pure water as starting solution that were carried out at 60 °C for 14 days, we also observed a higher Fe concentration in Mars-like reactors by a factor 2 for Fe and almost by two orders of magnitude higher for Mn. However, concentration of Fe in HO_2^+ is lower than the one in the witness experiment. For the HO_2^- experiment, Fe and Mn concentration trends appear to be correlated, with a first peak at 48 h followed by a decrease and a stable level until a second peak occurs around 250 h. Concentration trends for HO_2^+ are not correlated for Fe and Mn (similarly to AO_2^+) and follow a similar trend for Fe and Mn. The Fe concentration increases to a peak at 24 h and then decreases toward a stable low level after 72 h. Mn concentrations are increasing sharply and staying at a higher level for the rest of the experiment while having their absolute concentration equivalent to the low and stable level of the HO_2^- experiment. Concentrations in terrestrial witness WH are hard to correlate between Fe and Mn because of the extremely low

concentration of Mn. Fe concentration has a first peak at 24 h and a second peak around 100 h, with absolute values that are greater than in HO_2^+ while the only Mn concentration data point above the detection limit is at 24 h.

For the experiments starting with the acid solution, looking at both ambient and higher temperature runs, we observe a systematic correlation between Fe and Mn concentrations. Unlike the experiments starting with pure water, the concentration in the terrestrial witnesses are not significantly lower than that of the Mars-like reactor. No significant peak concentrations appear to be present in any of the runs, with concentration rapidly increasing to a stable and high level. In absolute values, concentrations in these experiments are at least two orders of magnitude higher than the one starting with pure water. For the runs at ambient temperature, $\text{A}\alpha\text{O}_2^-$ and $\text{A}\alpha\text{O}_2^+$ exhibit the same trend but the latter has 4 times lower concentrations for Fe and Mn, while having almost the same concentration as $\text{W}\alpha$. For the runs at higher temperature, the trends and the timing are similar with a maximum and steady concentration reached after 96 h, with absolute values almost equal to their equivalent at ambient temperature. $\text{W}\alpha$ might have slightly higher concentrations of Mn and Fe than $\text{W}\alpha$ and also have a limited peak in concentration around 100 h.

4.2. Analysis of the altered solids

Using the SEM coupled with EDS, we investigated the altered powder and built a general qualitative summary of the observed secondary phases elemental composition and their relative abundance derived from the SEM imagery (Table 4). We also report in the table the secondary phase assemblages that were collected in the filter (only when a deposit was observable), which are complementary to the data acquired on the altered powder and must be observed together to understand the run's mineralogy. In addition to the qualitative analysis, we also made stoichiometric identification of phases on the points that had the best quantification < 5% of other elements than those in the considered phase). The lateral resolution of the EDS technique is about 1 μm , with an interaction volume that is also 1 μm deep. Hence, any phases with dimensions equal or smaller than 1 μm would inevitably be affected by the composition of the mineral situated behind or around it. For the identification in Table 3, only protruding crystals or crystals that were thick enough were used for stoichiometric calculations. Their morphology were also chosen to be representative of other similar phases.

All the reported secondary phases are not exhaustive of what could be the complete phase assemblage and only give qualitative information of the major secondary phases that are forming. Nano phases or μm -scale phases could not be reported, even if widely present. Identification of minor phases such as clays would require a closer inspection, such as with the use of TEM, which was not possible to conduct for all samples, and was beyond the scope of our approach.

The main differences in phase assemblages between runs are driven by the variation in starting solutions. All the runs with acid in their starting solution have a higher degrees of alteration, consistent with the higher concentrations reported in the fluid, as well as S enrichment. The main elements present in the secondary phases are Fe, Ca, S and P. While EDS does not allow the direct identification of the valence state of Fe nor the quantification of the hydrogen abundance, stoichiometric calculations (including O) can be made to identify phases and differentiate oxides from other phases (Table 3). Unfortunately, as the samples are coated with carbon, it is not possible to have any formal identification of carbonates.

For the runs starting with pure water, no material was collected in the filter because no deposit was visible. Overall, these runs exhibit lower dissolution rates, with the minerals' surfaces being mostly free of dissolution pits and secondary phases compared to their acid counterparts 5. In ambient temperature runs, AO_2^- was generally more altered

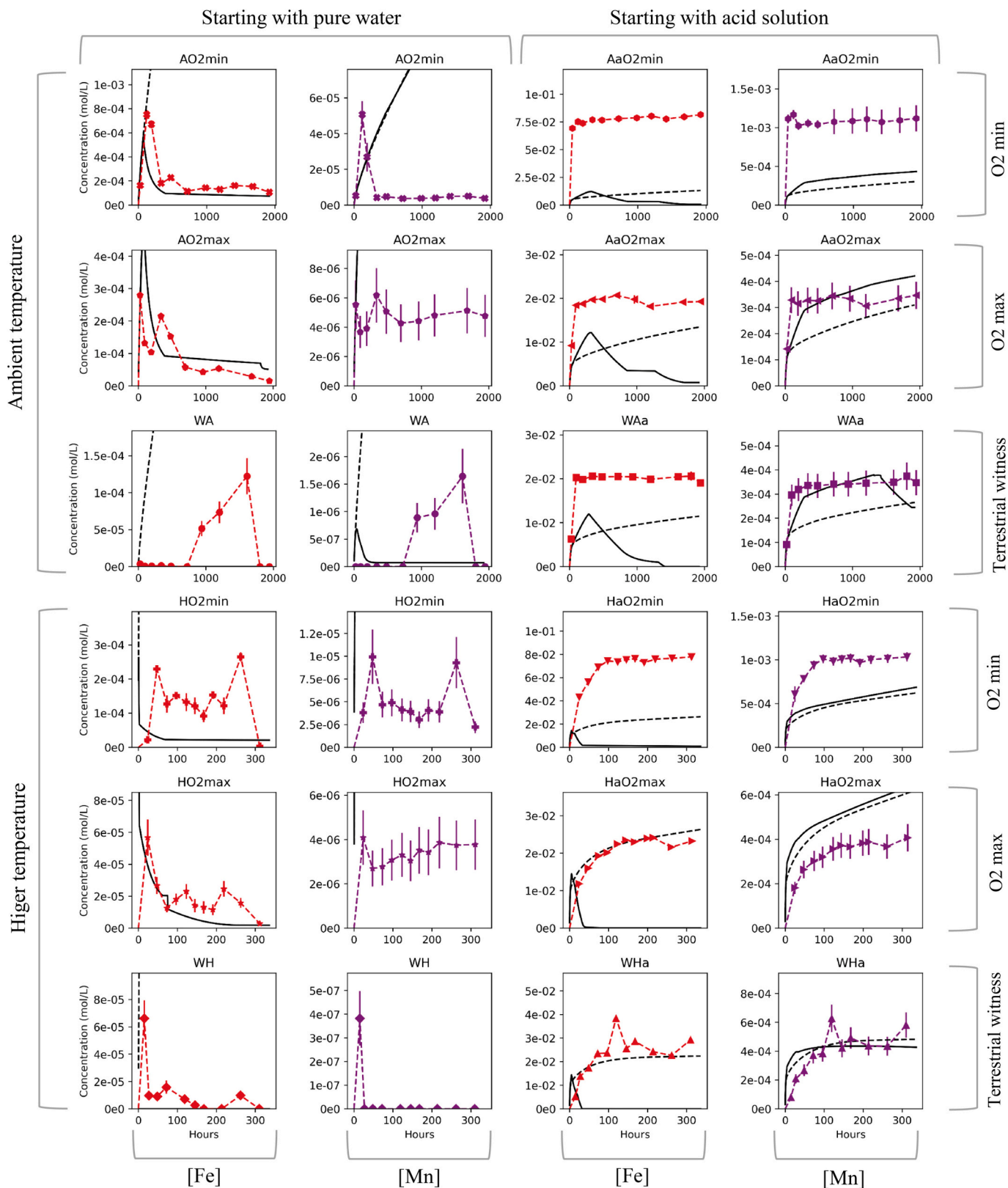


Fig. 4. Evolution of the total dissolved Mn and Fe concentration over time in the experiments and modeled concentrations. Experimental data are represented by points with Fe concentration in red and Mn in purple. Modeling results for kinetic dissolution and oxidation and thermodynamic precipitation “kdtp” are shown in solid black lines. Modeling results for kinetic dissolution only “kd” are shown in black dashed lines. When models overestimate by more than 1.5 times the maximum experimental concentration, the y-scale is set to 1.5 times this concentration. The plots are organized according to their experimental conditions with varying starting solutions, temperatures, and gas mixtures. The Table 5 helps to compare the experimental data with the models and this figure can be read with the corresponding modeled phase assemblage in Fig. 6. (For interpretation of the references to color in this figure legend, the reader is referred to the web version of this article.)

Table 3

Measured molar elemental ratios in the experiments where phases were identified. Each measurement corresponds to the best EDX spectra acquired on each mineral. S98, S226 and S24 EDS points can be seen located on SEM imagery in Fig. 5. The quantification of the corresponding spectra and other SEM imagery including S328 and S241 can be found in the supplementary material appendix B.

Experiment	O/Fe	O/S	S/Ca	Phase
AO2- (S98)	2.04	–	–	Goethite
AaO2- (S241)	–	8.08	1.17	Likely Gypsum
WAa (S226)	–	6.64	1	Gypsum
HaO2+ (filter, S328)	–	6.26	1.03	Gypsum
HaO2- (S24)	–	5.92	1.09	Gypsum

than AO_2^+ with sparse dissolution pits and a sparse secondary phase identified as Goethite based on stoichiometry and SEM imagery. AO_2^+ displayed extremely sparse dissolution pits, and we reported only a few possible secondary phases that are potentially Fe-rich, possibly including Al, P and S. For the HO runs, no significant dissolution morphology nor secondary phases were reported in HO_2^- . For HO_2^+ , extremely sparse iron oxide-like phases are reported. For both terrestrial witnesses WA and WH, no dissolution morphology nor secondary phases were observed. If some secondary phases have precipitated within the fluid in minor quantities, it is likely that they have been lost, especially in these experimental runs without acid in the starting solution.

For the acid runs, 4 filters were collected in addition to the altered powder. Filter material represents the fraction of the secondary phases

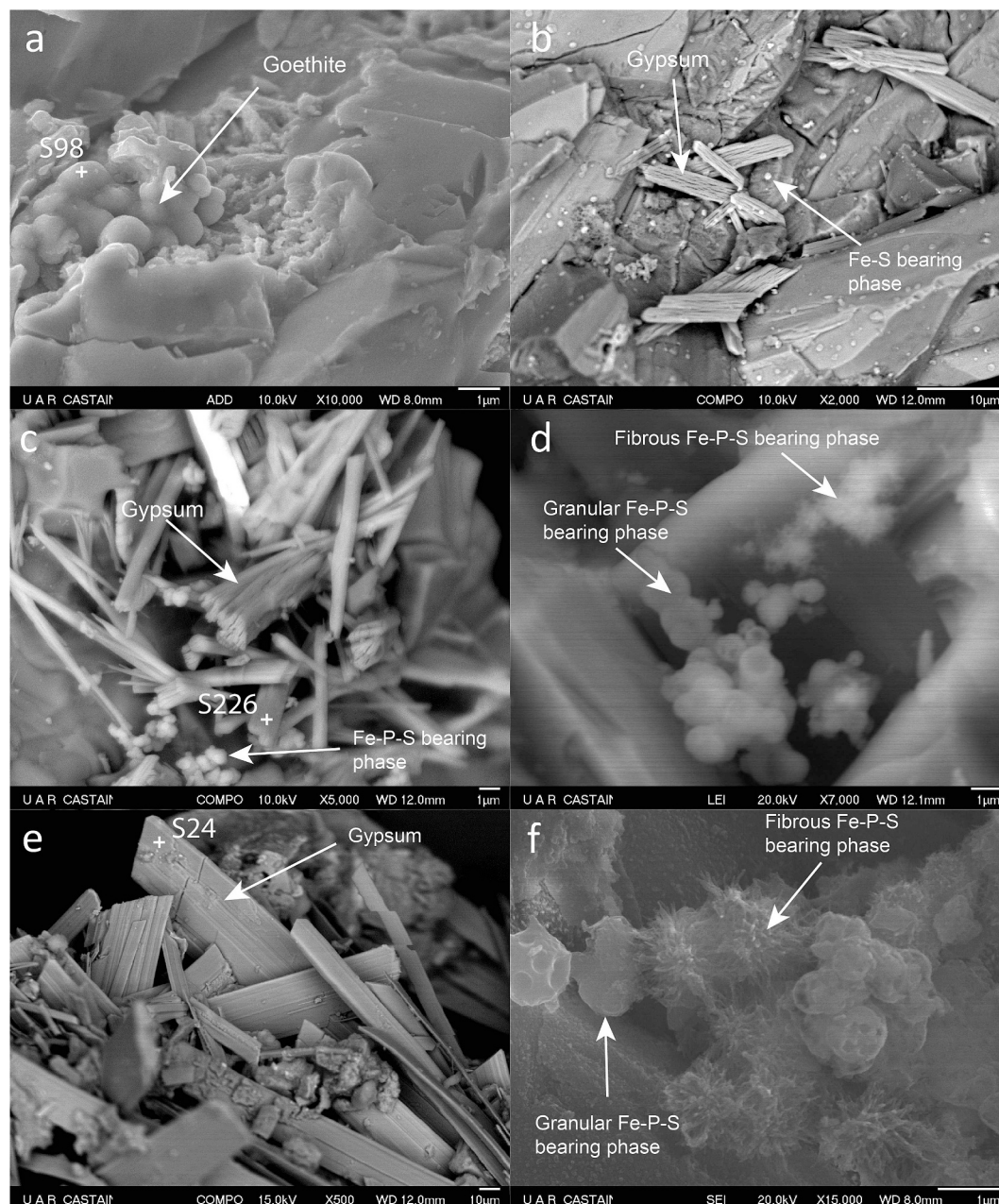


Fig. 5. SEM imagery of experiments (a) AO_2^- , (b) AaO_2^- , (c) WAa , (d) HaO_2^+ , (e) HaO_2^- , (f) WHa . The EDS points that were used for the stoichiometric calculations in Table 3 were added on the close-up SEM imagery. S24 was collected on similar crystals than in the (b) imagery, but the high resolution SEM image was preferred to show a close-up view. S328 was collected on large crystal in the filter material of HaO_2^+ . Other additional EDS spectra were also collected but not implemented to the image to make the visualization more practical. The SEM imagery, EDS spectra locations and spectra quantifications can be found in the supplementary material appendix B.

that was in suspension in some runs. This might also represent a fraction of secondary phases that had a reduced size or did not adhere enough to the primary mineral grains and was thus mobilized back in the fluid because of the turbulence created when pouring out the fluid from the reactors. This is supported by the complementary abundance of phases between filters and altered powders, as the runs in which the filter material was collected display less abundant secondary phases in the altered powder than in the filter. Therefore, beside $A\alpha\text{O}_2^+$, the runs that include filter results must be assessed together with the powders to understand the abundance and nature of secondary phases in the run.

For the runs at ambient temperature, we also observed abundant secondary phases in $A\alpha\text{O}_2^-$ with large Ca-sulfates crystals, identified as gypsum and smaller dispersed phases enriched in Fe, S and P (SEM picture a in Fig. 5). In $A\alpha\text{O}_2^+$, we observed that the secondary phases were more sparse than in $A\alpha\text{O}_2^-$. The identified secondary phases were also enriched in Fe, S and P and similar in morphology to the one in $A\alpha\text{O}_2^-$, however we did not identify any gypsum crystals. Contrary to $A\alpha\text{O}_2^-$ where no material was collected in the filter, the filter collected for $A\alpha\text{O}_2^+$ displayed abundant secondary phases, mainly composed of the same Fe-P-S enrichment identified in the altered powder. However, this is not the case for $A\alpha\text{O}_2^+$ powder that contains sparse secondary phases, but in which no filter material was collected. During the experiments, some solutions were clouded by colloidal-like material, which sometimes flocculated and settled. For $A\alpha\text{O}_2^+$, the suspension of fine colloids could have persisted and passed through the filter. The terrestrial witness $W\alpha\alpha$ had relatively abundant secondary phases, similar in quantity to $A\alpha\text{O}_2^-$, with developed Ca-sulfate crystals and spherical Fe-P-S phases. We noted that some of these spherical phases have grown on both the primary mineral surface as well as the Ca-sulfate crystals (Fig. 5). The filter for $W\alpha\alpha$ had even more abundant secondary phases, with fibrous agglomerates of Fe-P-S, but no Ca-sulfates, which might be link to the larger size of the Ca-sulfates compared to the Fe-P-S agglomerates. Among all the points collected on the Fe-P-S phase across different powders, we were able to collect 22 EDX spectra on 3 different sites in the filter material for $W\alpha\alpha$ and 14 spectra in the $W\alpha\alpha$ filter material that had cumulative totals of O-Fe-P-S >95% and qualified for potential stoichiometric identification. We observed in this dataset what appears to be a mixing line with a positive correlation for all elements (supplementary material appendix B). However, we could not formally identify any phase endmember with a known composition.

For the run at higher temperatures, we also observed abundant secondary phases. $H\alpha\text{O}_2^-$ altered powder displayed the largest gypsum crystal of all runs, with lengths up to 100 μm . We also observed in this run spherical phases embedded in an altered surface with Fe—S composition, but without any notable P associated. The primary phases were particularly altered, both in morphology and composition, but because of the substrate composition (EDX samples at depth up to 1 μm), no other secondary phases could be identified. We did not collect any filters for this run. In $H\alpha\text{O}_2^+$ powder, secondary phases were more sparse, and we did not observe gypsum crystals, but we did observe spherical and fibrous agglomerates of Fe-P-S. However, in the $H\alpha\text{O}_2^+$ filter, we observed abundant secondary phases, with gypsum crystals and Fe-P-S phases. In the witness powder $W\alpha\alpha$, we observed that the secondary phases were more abundant than in $H\alpha\text{O}_2^+$ but less than in $H\alpha\text{O}_2^-$. We identified sparse Fe enrichment, and Fe—P phase agglomerates. In the $W\alpha\alpha$ filter, we observed abundant secondary phases, with fibrous agglomerates and spheres of Fe-P-S phase. We could not identify any phases because of the signal of the substrate.

5. Models results and comparison to the experiments

To compare the experimental results and decipher the controlling parameters on Fe and Mn concentrations in each run, a summary table comparing models and experimental data was assembled (Table 5). This table compares the last data-points in the experiments that represents

the stable steady-state levels. The models compared are 1- kinetic dissolution and thermodynamic precipitation (kdtp), 2- kinetic dissolution (kd), 3- equilibrium of the primary phases with the initial fluid (equi 1), equilibrium of the primary and secondary phases with the initial fluid (equi 1 + 2). The “equi 1” and “equi 1 + 2” model details can be found in Section 3.2. The concentration values in green are within twice (2 factor) the measured data or twice below or above (2 factor) the instrument detection limit if the experimental data are 0. In orange, are the modeled data within the same order of magnitude (10 factor) from measured data or detection limit, and in red are the values beyond an order of magnitude.

Fig. 6 shows a visualization of the modeled phase assemblage comprising Fe and Mn and that results from the alteration in the “kdtp” model. The arrangement of the plot corresponds to the experimental conditions and is the same as in Fig. 4, reflecting the evolution of the modeled concentrations that are in solid black lines.

5.1. Controls on Fe concentration in experiments starting with pure water

In AO_2^- and AO_2^+ the evolution of Fe concentrations is divided into 3 phases (Fig. 4): 1- a steep rise of Fe concentration, controlled mainly by dissolution rates, but with a likely lower slope due to increasing oxidation and the start of oxide precipitation (lower than without oxidation), in addition to the hindered dissolution due to increasing Fe activities; 2- The concentration peak and decrease due to the oxide precipitation overcoming the inputs of Fe ions by dissolution; 3- the stabilization of the concentration in pseudo-equilibrium between dissolution and precipitation. This pseudo-equilibrium is supported by the comparison between the kinetics models and equilibrium models (Table 5): we see that for both AO_2^- and AO_2^+ , the final steady-state concentration is best explained by the kinetic dissolution and thermodynamic precipitation (kdtp) model, closer to the equilibrium concentration relative to the primary phases than the one relative to secondary phases. Hence, it is more likely that the final stable phase is controlled by the equilibrium between dissolution rates and oxidation rate.

Some discrepancies remain when comparing the modeled Fe phase assemblage (the precipitation of which induces [Fe] decrease in the model) to the experimental phase assemblage observed (Fig. 5, Table 4 and 6). Even if the AO_2^- and AO_2^+ modeled fluid evolution seems to fit the data, we only identified goethite but not any siderite in the altered powders. This might be related to the fact that EDX makes the identification of carbonates challenging because of the carbon coating of the sample (Section 4.2). However, it would still be possible to identify the carbonates based on the O/Fe ratios and their morphology, but this would require substantial amounts of carbonates for the sampling and quantification with EDX. The other and most likely explanation is that the model tends to artificially increase siderite precipitation, consistent with the fact that the model does not require any additional level of supersaturation for the phase to precipitate. Some previous experimental studies showed that a fair amount of supersaturation and alkalinity as well as circumneutral pH are required to precipitate siderite (Tosca et al., 2018). It is most likely that only goethite precipitated in observable amounts in our experiments. Similarly, the model seems to overestimate clays with large quantity of Mg-bearing hydrated nontronite (“Hnontronite(Mg)”) being produced. Even if it might be present in the experiments because a correlated decrease of [Al] observed in the fluid (supplementary material appendix C), it was likely only in extremely small amounts and were not observed in the solid. To precipitate observable quantities, much longer times would be required, as its precipitation kinetics are extremely low and generally favored in thermodynamic models because of its low solubility.

In the corresponding terrestrial witness $W\alpha$ (Fig. 4), the experimental oxidation peak is shifted in time, which would not be typically expected with higher $p\text{O}_2$ even if lower $p\text{CO}_2$ results in higher pH and slower dissolution rates compared to the Martian runs (Section 6.4). In

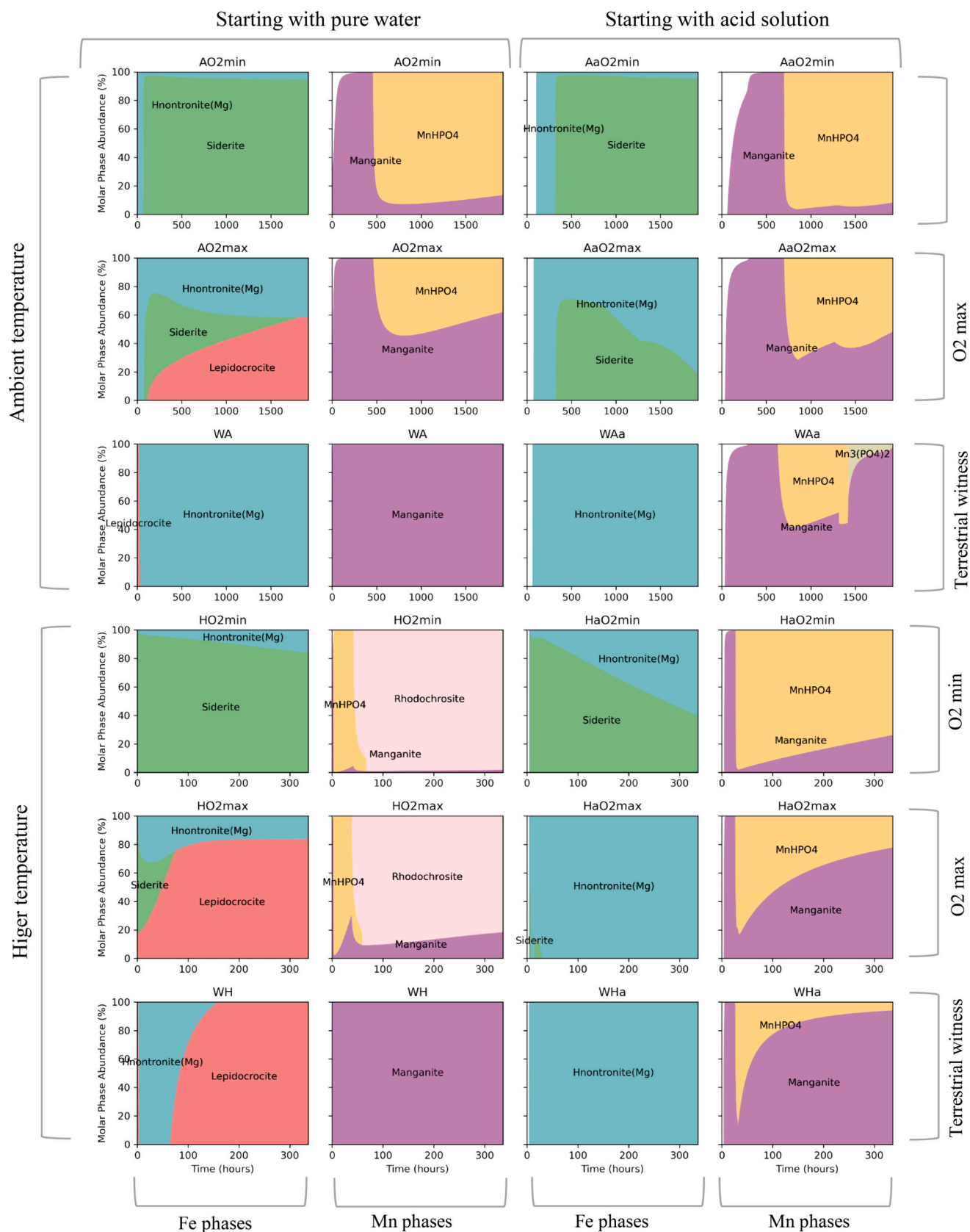


Fig. 6. Modeled phase assemblages with thermodynamic based precipitation (“kdtp”). The evolution of the proportion of the total molar quantity of Fe or Mn-bearing phases is displayed in colored area over time. Fe-oxide is “Lepidocrocite”, Mn-oxide is the “Manganite” and Mn-carbonate “Rhodochrosite” The grid arrangement is the same as in Fig. 4 and is meant to be compared with the modeling results of the “kdtp” (solid black line) in that figure. The predicted phase of the simulation in Fig. 8 can be compared with the phase assemblage obtained in for AO2 run.

Table 4

Qualitative summary of identified elements in secondary phases. The qualitative denotations represents the overall phase assemblage. No detections “-” (grey), Likely “~”(light salmon), rare “+” (light yellow), sparse “++” (light green), common “+++” (dark green), major “++++” (dark green).

Sample	Fe-bearing	Ca-bearing	Al-bearing	S-bearing	P-bearing
AO2- Alter	+	-	-	-	-
AO2+ Alter	~	-	~	~	~
WA Alter	-	-	-	-	-
HO2- Alter	-	-	-	-	-
HO2+ Alter	+	-	-	-	-
WH Alter	-	-	-	-	-
AaO2- Alter	~	++	-	++	-
AaO2+ Alter	+	-	-	+	+
AaO2+ Filter	+++	-	-	+++	+++
WAa Alter	+	+++	-	++	+
WAa Filter	+++	-	-	+++	+++
HaO2- Alter	+++	++++	-	++++	~
HaO2+ Alter	+	-	-	+	+
HaO2+ Filter	+++	+++	-	+++	+++
WHa Alter	+++	-	-	++	++
WHa filter	++++	-	-	++	++

the “kdtP” model, the fluid evolution is at a constant value below detection limit (Fig. 4, the black line is not visible because almost merged with the x axis), because the model predicts a much faster buffering (increase of pH and activities caused by dissolution), resulting in faster oxidation rates. This is consistent with the likely overestimated amount of secondary phases of the model, as no secondary phases were identified in the altered powder (Fig. 6 and Table 4). In addition, Hnontronite(Mg) is the main phase precipitating in the model, quickly overcoming the initial Fe-oxide precipitation (Fig. 6). If we assume that because of their precipitation kinetics much less clays did precipitate, the “kd” model still vastly overestimates the dissolution (Fig. 4). The most likely reason for the observed concentration peak that is shifted in

time is the overestimation of the early dissolution that causes an almost immediate removal of Fe by enhanced activity and pH-driven oxidation. For the final phase, both the “kdtP” and “equi 1 + 2” models are predicting concentrations that are close or below the detection limits, which is consistent with the below detection limit [Fe] controlled by the thermodynamic equilibrium of Fe-oxide (Table 5).

For the runs at higher temperatures, the overall [Fe] are lower in HO_2^- and HO_2^+ than at ambient temperature in AO_2^- and AO_2^+ . Even if dissolution rates are theoretically about 6 times faster at 60 °C, the observed [Fe] peak is shifted earlier in time by less than a factor 2 (Fig. 4). The modeled peak is still reached much faster than the one measured. Even if the dissolution rates increase with temperature, the

Table 5

Comparative table of the last data-points from experiments and models. The last data-points for Fe (Fe XP) and for Mn (Mn XP) are the reference for the experiments and represents the pseudo-equilibrium or steady-state levels. The models compared are 1- kinetic dissolution and thermodynamic precipitation (kdtP), 2- kinetic dissolution (kd), 3- equilibrium of the primary phases with the initial fluid (equi 1), equilibrium of the primary and secondary phases with the initial fluid (equi 1 + 2). Concentration values in green are within twice (2 factor) the measured data or below the instrument limit of detection (LOD) if the reported data are 0. In orange, are the modeled data within the same order of magnitude (10 factor) from measured data or detection limit, and in red are the values beyond an order of magnitude.

	AO2min	AO2max	WA	HO2min	HO2max	WH	AaO2min	AaO2max	WAa	HaO2min	HaO2max	WHa
Fe XP	1.10×10^{-4}	1.83×10^{-5}	< LOD	6.55×10^{-6}	5.82×10^{-6}	3.12×10^{-6}	8.16×10^{-2}	1.93×10^{-2}	1.91×10^{-2}	7.79×10^{-2}	2.33×10^{-2}	2.93×10^{-2}
Fe (kdtP)	7.47×10^{-5}	5.13×10^{-5}	4.11×10^{-11}	2.11×10^{-5}	1.81×10^{-6}	2.71×10^{-10}	7.50×10^{-4}	7.47×10^{-4}	1.65×10^{-7}	1.01×10^{-3}	3.85×10^{-5}	1.30×10^{-6}
Fe (kd)	6.79×10^{-3}	6.71×10^{-3}	1.01×10^{-3}	2.44×10^{-2}	2.43×10^{-2}	4.64×10^{-3}	1.32×10^{-2}	1.34×10^{-2}	1.15×10^{-2}	2.64×10^{-2}	2.63×10^{-2}	2.24×10^{-2}
Fe (equi 1)	8.16×10^{-4}	8.91×10^{-4}	1.20×10^{-9}	3.28×10^{-6}	3.56×10^{-6}	4.60×10^{-6}	6.53×10^{-4}	7.14×10^{-4}	8.67×10^{-7}	2.66×10^{-6}	2.90×10^{-6}	2.25×10^{-6}
Fe (equi 1+2)	2.85×10^{-9}	2.67×10^{-9}	4.50×10^{-11}	1.10×10^{-10}	1.04×10^{-10}	9.20×10^{-10}	1.02×10^{-9}	9.23×10^{-10}	5.94×10^{-12}	1.41×10^{-10}	1.37×10^{-10}	4.72×10^{-11}
Mn XP	3.75×10^{-6}	4.76×10^{-6}	< LOD	2.22×10^{-6}	3.78×10^{-6}	< LOD	1.12×10^{-3}	3.47×10^{-4}	3.47×10^{-4}	1.03×10^{-3}	4.08×10^{-4}	5.81×10^{-4}
Mn (kdtP)	1.52×10^{-4}	1.32×10^{-4}	6.91×10^{-9}	1.21×10^{-4}	1.17×10^{-4}	6.32×10^{-7}	4.33×10^{-4}	4.21×10^{-4}	2.45×10^{-4}	6.87×10^{-4}	6.48×10^{-4}	4.27×10^{-4}
Mn (kd)	1.46×10^{-4}	1.44×10^{-4}	2.34×10^{-5}	5.58×10^{-4}	5.56×10^{-4}	1.68×10^{-4}	3.04×10^{-4}	3.10×10^{-4}	2.66×10^{-4}	6.22×10^{-4}	6.22×10^{-4}	4.82×10^{-4}
Mn (equi 1)	2.34×10^{-3}	2.34×10^{-3}	1.09×10^{-3}	2.34×10^{-3}	2.33×10^{-3}	4.03×10^{-4}	2.34×10^{-3}	2.34×10^{-3}	1.32×10^{-3}	2.33×10^{-3}	2.33×10^{-3}	6.63×10^{-4}
Mn (equi 1+2)	1.89×10^{-8}	8.84×10^{-9}	2.36×10^{-11}	6.61×10^{-8}	3.08×10^{-8}	2.04×10^{-8}	2.70×10^{-7}	1.37×10^{-7}	3.71×10^{-11}	3.24×10^{-6}	1.65×10^{-6}	1.19×10^{-9}

oxidation rates and precipitation rates also increase with temperature, which might limit [Fe] in the solution. Another explanation could be the underestimation of activation energies and therefore overestimation of the temperature dependencies, as demonstrated by the “kd” model, which vastly overestimates the concentration of Fe and Mn (Table 5). Moreover, the lack of precipitation kinetics can induce a much faster decrease (overly optimistic precipitation of clays) as well as the overestimation of siderite precipitation. Another factor to consider is the lower solubility of oxygen at higher temperatures. However, it seems that this does not interfere with the oxidation rates, with a measured average dissolved oxygen similar between “H” and “A” experiments (supplementary material appendix C).

The evolution of Fe and Mn follow similar trends in HO_2^- and HO_2^+ as in AO_2^- and AO_2^+ , with the exception of a second peak of [Fe] at the end of the second week for the HO_2^- experiment (Fig. 4). The models predict an almost immediate peak and decrease of [Fe] followed by a stable and low concentration for both HO_2^- and HO_2^+ . Explaining the second Fe peak is challenging: a second increase in [Fe] would mean that we have an increase in dissolution or a hindered precipitation of Fe-bearing secondary phase. A possible explanation might be that another phase starts to precipitate at a lower rate than the previous Fe-phase. The second peak of [Fe] is correlated to the [Al] peak (supplementary material appendix C), which might be consistent with a Fe-bearing clay precipitation. In the last pseudo-equilibrium phase, we see that the closest values are predicted by the “equi 1” and “kdtp” models. This would mean that the final concentration would be close to equilibrium from the initial solution and starting rock. Nonetheless, as the “kdtp” model is close to the measured [Fe], and that the model “equi 1 + 2” predicted much lower [Fe], the steady-state equilibrium between dissolution and oxidation/precipitation of Fe-oxide might be similar.

The behavior of [Fe] is rather different between WA and WH from the comparison between the “H” and “A” Martian runs. The oxidation peak in WH is reached much faster than in WA, and at a much lower concentration (Fig. 4). This much earlier peak could mean that in the absence of $p\text{CO}_2$ and higher pH, the temperature dependencies of the oxidation rate would dominate and shift the peak earlier. As for the concentration, higher oxidation rates might limit the [Fe]. Unlike in HO_2^- and HO_2^+ , the solubility starts to be limiting under higher $p\text{O}_2$, as seen in the measured dissolved oxygen, which is on average lower in WH than in WA (supplementary material appendix C). However, the slightly lower dissolved O_2 does not appear to limit the oxidation rate much. Similar to the WA, the final concentration is also under the detection limit, and both the “kdtp” and “equi 1 + 2” models are close to the detection limit (Table 5).

In our experiment, the oxygen parameter induced little variation in the redox behavior of the experiment or observed phase assemblage. On the other hand, slightly higher $p\text{CO}_2$ could cause higher dissolution rates and concentration (Table 2). The long-term control of the ambient temperature series appears to be a dynamic rate equilibrium between dissolution, oxidation and precipitation, with dissolution rates being the main limiting factor. The higher temperature increased all the rates, causing lower peak concentrations as well as lower final concentrations. Long-term control is close to the equilibrium relative to primary phases (Table 5), but is likely slightly higher because of the close but similar concentration due to the rate of precipitation. The effects on the phase assemblage might become greater at lower $p\text{O}_2$, while still being considered oxidizing in a thermodynamic only pH-eH space.

5.2. Controls on Mn concentration in experiments starting with pure water

We did not report any Mn-bearing phases in the altered powder: this was expected due to the initial low bulk proportion of Mn that would result in extremely low quantities of Mn-bearing phases. For this reason, we will mainly rely on the fluid analysis and the model. In most of the

experiments, increase of [Mn] is correlated with the increase of [Fe]. As both elements are carried by the same dissolving minerals (olivine and pyroxene), this is an expected consequence. As it is for [Fe], higher [Mn] peaks are correlated with higher $p\text{CO}_2$, and “H” runs peaks are lower than “A” runs. However, both Martian runs at higher $p\text{O}_2$ do not exhibit a clear peak and seem to stabilize directly at similar concentrations in the pseudo equilibrium stable level. Because of its intrinsic low kinetic rates, Mn oxidation could not be fast enough to cause a significant decrease of [Mn] (and thus form a peak of concentration) with the same timing as Fe-oxidation. Modeled phase assemblage predicts Mn-oxide, and depending on temperature, manganese phosphate or carbonates (Fig. 6). However, their precipitation does occur only in extremely limited quantities, which translates in almost no differences between the “kdtp” and “kd” models, both overestimating the [Mn] (Fig. 4). Moreover, in all the experiments, witnesses included, when a decrease of Mn concentration is observed, it is always correlated with Fe concentration. A possible explanation for the Mn concentration decrease could be the sorption of Mn onto the newly formed Fe-oxides. However even if Fe-oxide can adsorb Mn(II) at a pH and temperature range compatible with our experiments, the adsorption capacity of goethite alone could not explain the observed drop in concentration (Kan et al., 2013). Another possibility could be a surface catalysis of the Mn oxidation by Fe-oxides or even by auto-catalysis onto newly formed Mn-oxides, but we cannot have a good constraint on available surfaces (Martin, 2005; Lan et al., 2017). Alternatively, even if the model did not predict its precipitation and that it was not observed, minor quantities of Ferrite (Mn), which is formed with Fe(III) but integrates Mn(II) in its structure, could explain the observed correlation.

Unlike for [Fe], the final [Mn] in all Martian runs are similar and all 4 models either overestimate or underestimate them. The final concentrations in these experiments are two orders of magnitude lower than both “kdtp”, “kd” and “equi 1” models, while being two orders of magnitude higher than the “equi 1 + 2” models which would be caused by Mn-oxide equilibrium (Table 5). The comparison with the mostly accurate description of [Mn] in the acid runs (Section 5.3) supports that in experiments starting with pure water, a Mn removal mechanism is missing in the model and/or that no or extremely sparse Mn-oxides are formed compared to an equilibrium model, while the rate of this mechanism is sufficient to lower the concentrations compared to the “kd” model. Thus, the controlling factor on the stable level of Mn appears to come from the steady-state equilibrium between the dissolution rates (release of Mn^{2+}) and one or a combination of mechanisms as cited above. The lack of peaks in higher $p\text{O}_2$ runs might be linked to a higher production rate of Mn oxide and potential catalysis due to increased $p\text{O}_2$ and/or the slightly lower $p\text{CO}_2$ (Table 2), increasing adsorption/catalysis efficiency.

In the witness runs, while the peak concentration seems to also be linked to the same unidentified mechanism, final [Mn] are much closer to the concentrations that are modeled and caused by Mn-oxide precipitation. The final concentrations are below the detection limit, which is compatible with the estimation of the “equi 1 + 2” and “kdtp” models. This is consistent with a concentration mainly controlled by the slower (compared to Fe) but steady oxidation rate and formation of Mn-oxide, consistent with the modeled phase assemblage. On Earth, [Mn] in oxygenated rivers and streams is higher than its equilibrium concentration, and therefore kinetically controlled by its slow oxidation rate. Reported values in rivers and streams are around the detection limit of our instrument with concentrations as low as $5.8 \times 10^{-8} \text{ mol L}^{-1}$ (Laxen et al., 1984). This corresponds to the “kdtp” modeled value, which is much higher than the equilibrium value “equi 1 + 2” of about $2 \times 10^{-11} \text{ mol L}^{-1}$. Therefore, we propose that in the WA experiment, [Mn] is in a pseudo-equilibrium state between the dissolution rates and oxidation rates. This is consistent with the similar timescales between our experiments and water residence time in terrestrial rivers and streams.

5.3. Controls on Fe and Mn concentration in experiments starting with acid solutions

In the experiments starting with the acid solutions, the variations of Fe and Mn concentrations are much less variable than in pure water experiments. On the other hand, many more secondary phases were produced because of the increased dissolution rates. In all the experiments, both Fe and Mn concentrations increased steeply and stabilized rapidly at a constant level (Fig. 4). Evolution of [Fe] is best described by the “kd” model, while the “kdtP” model seems to overestimate clay precipitation (Table 5), as evidenced by the absence of clays in the altered powders (Table 4). As discussed in Section 6.4, shifts in concentration within an order of magnitude is likely due to SA variation between the theoretical derived value and the measured BET value. The [Mn] concentration is also well explained by the “kd” model. Unlike for [Fe], the “kdtP” model is also close to the experimental data, even if in the later Mn-oxide and phosphate are modeled (Fig. 6), but only in negligible quantities. The final concentrations are best explained by the “kd” model for Fe and Mn as well as “kdtP” for Mn. This means that even with secondary phases forming, concentrations are mainly controlled by the dissolution rates. These dissolution rates are mainly controlled by the acidity, with increase of concentrations having the same timing independent of the temperature.

The concentrations are higher and similar in $A\alpha O_2^-$ and $H\alpha O_2^-$, which are the experiments with slightly higher pCO_2 (Table 2). However, while $A\alpha O_2^+$ and $H\alpha O_2^+$ have similar concentrations, their values are strikingly similar to the witnesses $WA\alpha$ and $WH\alpha$ despite their rather different pCO_2 . This means that pCO_2 cannot only be the factor explaining the higher concentrations in both $A\alpha O_2^-$ and $H\alpha O_2^-$. Another potential controlling parameter could be the pO_2 of the O_2^- runs that is much lower than in the other runs. These parameters might influence the redox sensitive Fe and Mn bearing phases. Observed phases included large crystals identified as gypsum (Table 3) and a phase or mixture of phases composed of Fe, P and S (Table 4, supplementary material appendix B). The measured pH for O_2^- experiments is the lowest of all (pH 1), and does not increase significantly over time, unlike the O_2^+ experiments, where it increases from 1 to 3 (supplementary material appendix C). In the kinetic model with precipitation, gypsum is correctly modeled but clay precipitation is once again overestimated due to the lack of precipitation kinetics and higher modeled pH. Without this clay precipitation, phosphates such as variscite ($AlPO_4 \cdot 2H_2O$) or woodhouseite ($CaAl_3(PO_4)(SO_4)(OH)_6$) could potentially be stable, and closer to what could be the actual secondary phase(s). Lower pH is unexpected as higher concentrations are generally linked to increased buffering and higher pH. Reconstruction of the pH with the final measured concentration yield pH estimates around 5. A possible explanation is passivation of the mafic mineral surface, so after the initial explosive phase, no further dissolution occurred and precipitation of phases released protons lowering the pH (Gil-Lozano et al., 2024). Alternatively, we can hypothesize that the other runs went through a cycle of dissolution and precipitation, further consuming the primary minerals but leaving a lower stable concentration.

6. Extrapolation and discussion: the ancient Mars aqueous environment

6.1. Relevance of batch reactions in a Martian open system

Before applying the results of batch reaction experiments and models to the ancient Mars conditions, we have to understand how the experimental parameters compare to those found in a natural system. Despite our efforts to close the gap between the experiments and the natural parameters, some discrepancies remain. The pO_2 parameter of our experiment is likely much higher than that of the average ancient Mars: even though the maximum pO_2 value was extrapolated from an ancient

Mars atmospheric model (Wordsworth et al., 2021), it would have been only episodic. The present day Mars atmosphere contains around 1500 ppm of O_2 and is produced mainly by H_2O and CO_2 photolysis (Krasnopolsky, 2017). Some studies propose that if Mars' warming was caused by high pH_2 , the current Mars pO_2 would be the highest in its history (Wordsworth et al., 2017). When applying the results of our experiments and models to Mars, it is therefore necessary to also consider lower pO_2 values.

The reactive surface would have a huge influence on the time scales and concentration of the fluids. However, natural SA would depend on the grain size distribution from very fine and very reactive to coarse and poorly reactive. Mars sedimentary rocks provide evidence for a wide variety of grain sizes including a large number of mud size sediments within Gale crater ancient lake basin strata (Rivera-Hernández et al., 2020). The reactive surface of our experiments is similar to fine sand in terms of granulometry, with a total geometrical reactive surface of around $0.016 \text{ m}^2 \cdot \text{g}^{-1}$ and BET derived of $0.18 \text{ m}^2 \cdot \text{g}^{-1}$. If we consider that most of the pristine rock that later interacted with liquid water came from periglacial erosional processes, their grain size could be comparable to terrestrial glacial collovium. Unlike other erosional processes (besides wind), this mechanical-only process is capable of producing a very fine grain size. From the grain size distribution reported on terrestrial collovium and using the Hodson formula, a reactive surface area of the toeslope would be around $0.6 \text{ m}^2 \cdot \text{g}^{-1}$ (Hodson, 2006; Sowiński, 2016). If the finer part was quickly dissolved, the later pseudo-equilibrium steady-state concentration would result in SA comparable to that of our experiment. Alternatively, if we consider that the steady-state SA is stable as the sediments are renewed, the average SA could be at least an order of magnitude higher than in our experiment. Alternatively, if we assume that the watershed was not characterized by an abundance of fine sediments, but rather by unaltered volcanic rocks, the reactive surfaces could be significantly reduced.

Our experiments only lasted for about 3 months; however, even for short-lived aqueous activity on Mars, the hydrological system could be active for centuries at least. On the other hand, surface water in direct contact with the atmosphere would have residence times much shorter than the total duration of the system (Goddéris et al., 2006). Therefore, it is unlikely that the same rock reacts with the same fluid for extended periods within an open system compared to the overall life of the system. In addition to the renewal of the fluid, the source-to-sink sedimentary system would result in fresh rock that is constantly exhumed, while more altered rocks are isolated from the system in the sedimentary sink, advocating for renewal of the starting material as well. Longer interaction times would be typically expected in closed systems at low W/R, and in geological terms, pore water with no direct contact with the atmosphere and no water fluxes. In a reactive transport model, our experiment would be the equivalent of a single reactive cell with a rather low flux of water and high porosity, considering both time and W/R.

The tested temperatures are 23°C and 60°C . If 60°C is unlikely for fluids in direct contact with the atmosphere, besides some hydrothermal resurgences, 23°C might be a reasonable estimate. The surface temperatures could also have been much lower, as 23°C on average is high even compared to the terrestrial global average of 15°C . If Mars conditions were likely at lower temperatures, with average just above freezing, all the kinetics rates will slow down, counterbalancing other parameters, such as higher reactive surfaces.

Evidence in the Gale crater on Mars showed that the alteration inherited from the open system was not strong enough to entirely overprint the composition of the source rock, implying low weathering rates in the open system (Bedford et al., 2019; Mangold et al., 2019). In addition, there are now numerous rock samples with alteration mineral assemblages out of equilibria pointing to water-limited reactions within the sediments (Vaniman et al., 2018; Bristow et al., 2021).

6.2. Inferred mobility of Fe and Mn in Martian conditions

We modified our kinetic alteration model to better predict the phase assemblage obtained in the experimental results starting with pure water. We modified the conditions of siderite precipitation by implementing the experimentally reported supersaturation level that was reported for effective precipitation (Tosca et al., 2018), as confirmed considering the absence of siderite in our experiments. Furthermore, because we concluded from our experiments that the precipitation of clays was vastly overestimated because of their low solubility and the absence of precipitation kinetics; they were removed from the list of potential phases. With this modified model, we performed a sensitivity test with 3600 simulations (60×60 grid) in the $p\text{CO}_2 / p\text{O}_2$ space through time. Each simulation was integrated over 500 time steps, which were required to resolve finer variations of concentration due to the multiple kinetic rates. The range of $p\text{O}_2$ was set from 10 ppm oxygen to 300 mbar (10% at 3 bar total pressure) and the $p\text{CO}_2$ from the present

day Martian pressure (6 mbar) to 3 bars. Two sets of runs were performed: one with the same experimental conditions as the AO_2 runs, and another with a reduction in the reactive surface area (SA) by two orders of magnitude and an increase in time of around two orders of magnitude, lasting 20 years. As discussed in Section 6.1, the time dimension must be interpreted as a residence time. Therefore, runs at 1/100th over 20 years represent a low end of what would be a weathering reaction in direct contact with the atmosphere. We also note that if this fluid is cut off from direct equilibrium with the atmosphere, the remaining dissolved O_2 and CO_2 in groundwater will vary due to subsequent oxidation / precipitation, but it will not reflect a change in atmospheric composition. Adjustment on Mn oxidation and precipitation could not be implemented; therefore, although it will not change the overall behavior, the initial concentrations of Mn might be overestimated.

The Fe and Mn concentrations resulting from the sensitivity test are presented in a 3D space with x axis as the $p\text{CO}_2$, y axis as the $p\text{O}_2$ and z axis as the time (or residence time) (Fig. 7). We observed that:

Fe²⁺ concentration in the $p\text{CO}_2$, $p\text{O}_2$ and time space

Mn²⁺ concentration in the $p\text{CO}_2$, $p\text{O}_2$ and time space

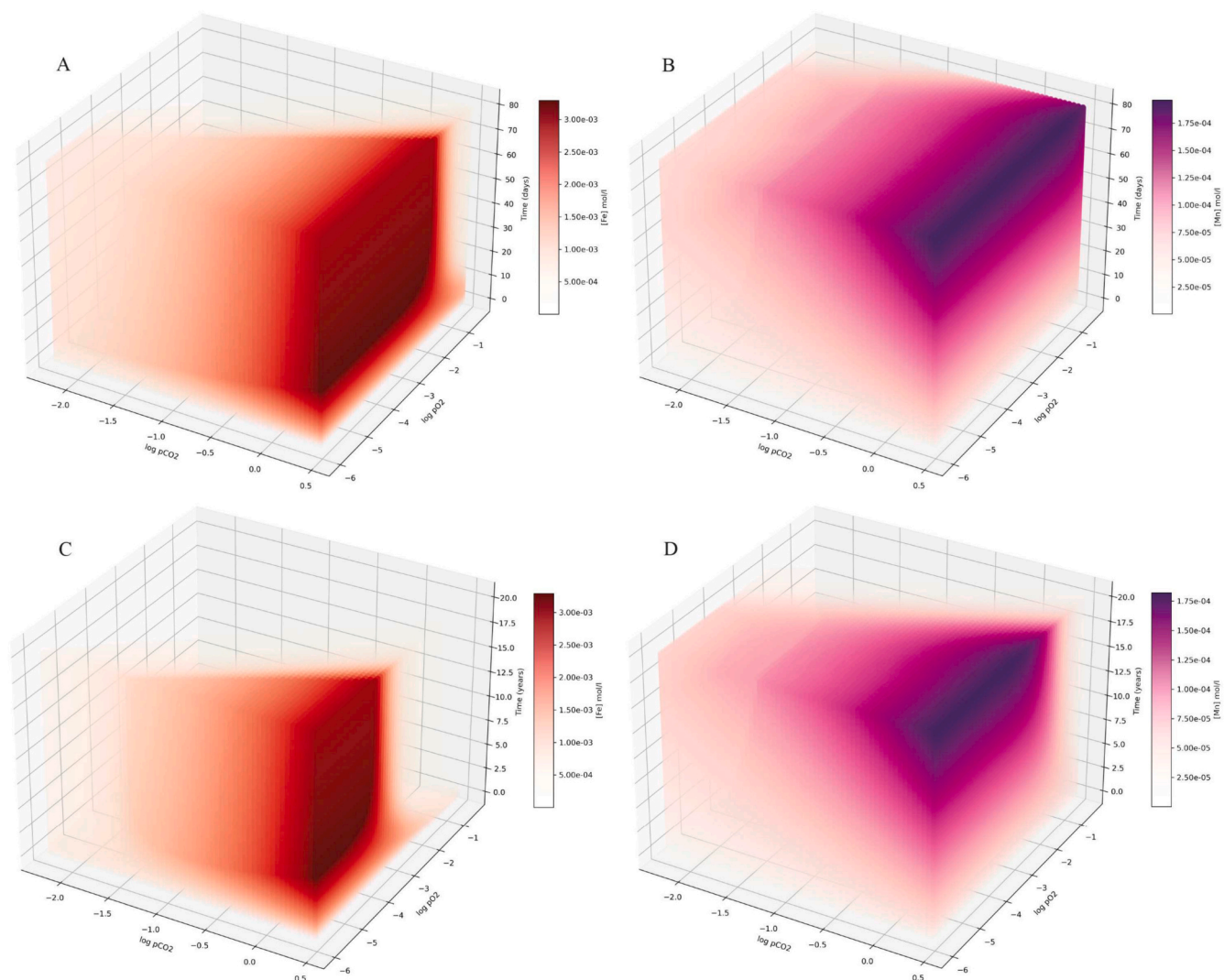


Fig. 7. Sensitivity test of our kinetic alteration model. The results of the simulations are presented in a 3D space with x axis as the $p\text{CO}_2$, y axis as the $p\text{O}_2$ and z axis as the time (or residence time). The intensities of the colors, red for Fe and purple for Mn represent the concentrations. When concentrations tend to 0, the points are faded or transparent to help visualization. Evolution of Fe (A) and Mn (B) concentrations with the same experimental conditions as AO_2 runs. Evolution of Fe (C) and Mn (D) concentrations with the same temperature and starting solution as AO_2 runs, but 1/100th of the SA and over 20 years. To help visualize the effect of precipitation on concentration, (A) and (B) final concentrations (top face of the cube) can be compared with the Fig. 8. The ancient Mars atmosphere was likely above -1 in $p\text{CO}_2$. (For interpretation of the references to color in this figure legend, the reader is referred to the web version of this article.)

1. Fe and Mn concentrations increase with longer times (increased buffering/higher weathering rates), higher $p\text{CO}_2$ (pH-driven increase in weathering rates and lower oxidation rates) and lower $p\text{O}_2$ (lower oxidation rates).
2. Both Mn and Fe can be mobile even under oxidizing conditions, with the transition from “oxidizing” to “reducing” conditions (relative to concentration and mobility, at any $p\text{CO}_2$) reached at $p\text{O}_2 = -6$ for Fe (in C) and $p\text{O}_2 = -3$ for Mn (in D). For comparison, in the equilibrium model, Fe can be oxidized down to $\log p\text{O}_2 = -50$, and the lowest $p\text{O}_2$ in this simulation is only -6 .
3. Mn mobility is much greater than Fe mobility due to its much lower oxidation rate, and its mobility is more directly controlled by $p\text{CO}_2$ (through pH) than by $p\text{O}_2$ (highest Mn concentration in B and D at highest $p\text{CO}_2$ and longest time).
4. The reactive surface area appears to control the mobility boundary (diagonal transition boundary between high and low concentrations in A, C and D in Fig. 7) through $p\text{O}_2$ and $p\text{CO}_2$, while the variable residence time locally controls mobility.

The only scenario in which Mn is less mobile is in (D) (with low SA and longer time), at high $p\text{CO}_2$ and $p\text{O}_2$ values and after enough time, or at low $p\text{CO}_2$ and moderate $p\text{O}_2$ after enough time, allowing buffer-driven oxidation (higher pH and activities) to occur. For Fe, its mobility remains high even after the concentration peak formed by siderite precipitation (visible in A and C at the highest intensities of red) at lower $p\text{O}_2$ and higher $p\text{CO}_2$. At higher $p\text{O}_2$, looking at a vertical time profile (for example in C at $p\text{CO}_2 = 0.5$ and $p\text{O}_2 = -2$) we observe an initial increase in concentration followed by a smoother decrease (fading red) of the concentration toward extremely low Fe concentration, advocating for much lower mobility after sufficient time.

While kinetically controlled in a Martian open system, Fe might be partially oxidized and form authigenic Fe-oxides, while being relatively mobile compared to Earth. Therefore, Fe and Mn are most likely to be leached and could precipitate only in later diagenetic stages or by evaporation. In Gale crater, the Curiosity rover has discovered several features indicative of iron mobility. In the Vera Rubin Ridge (VRR), observation of Fe-oxide enrichment showed that the initial reducing fluids preferentially mobilized Fe and Mn. While the origin of the oxidant remains under discussion, this demonstrated that differential redox are capable of mobilizing Fe and Mn without clear evidence of in-situ alteration of other minerals (David et al., 2020). Although not related to open system alteration or linked to the atmosphere, this also shows in-situ evidence of differential deposition of Mn and Fe due to their difference in pH/eH conditions and associated kinetics (Frydenvang et al., 2020).

The source and oxidant type as well as the associated conditions remain under discussion to explain the oxidation of reduced Fe(II) and Mn(II). Under an open system alteration on Mars, with O_2 as the oxidant, we showed that Fe-oxide production is possible even at moderately low $p\text{O}_2$ by steady-state chemical sedimentation from a lake with moderate concentrations (Loche et al., 2022).

Moreover, during weathering, modeling results show that Fe and Mn have a differential mobility due to their kinetics, with a partial precipitation of Fe-oxide (Loche et al., 2023). In our sensitivity test, we confirm differential mobility in a range of $p\text{CO}_2$, $p\text{O}_2$ and residence time. This differential mobility was supported by the measured preferential depletion of Mn in a mudstone unit bearing geochemical evidence of leaching (Berger et al., 2022).

The experimental results and the comparison with the models confirmed that only a partial removal of Fe occurred and that Fe concentrations were higher than what they should be at equilibrium (Table 5). The Mn concretions and fracture fills observed on Mars appear to have been detected in both oxidized and reduced form (Lanza et al., 2016; Meslin et al., 2018; Treiman et al., 2023). The formation of Mn-oxide is challenging to explain with O_2 on the surface of Mars due to the low pH induced by the high $p\text{CO}_2$ and under a reasonable residence

time. The experiments also showed that there was a relationship between the Mn concentration and the Fe concentration, with decrease of Fe correlated with decrease in Mn. Although it is not clear which mechanism was involved, we can hypothesize that because of slower Mn oxidation and under a flux of water, a front of Fe-oxide would precipitate, while an increasingly Mn-rich and Fe-poor fluid would be spatially separated from Fe-oxides, resulting in greater Mn mobility by preventing Mn scavenging by the unidentified catalysis/adsorption mechanism linked to Fe-oxides. In a closed system, with higher buffering and higher pH, Mn oxidation would be more favored, but due to differential oxidation rates with Fe, most of the dissolved O_2 would be quickly consumed by Fe-oxide precipitation, effectively creating a reducing fluid with high Mn(II) concentration remaining. To keep O_2 as a potential oxidant, the late stage Mn-rich fluid should be in direct contact with an oxidant source such as the atmosphere and have a sufficiently high pH, typically above 8 to achieve significant oxidation (Morgan, 2005). A possible pathway could be that the pH can increase during evaporation, which would greatly enhance the oxidation rate, but this pathway depends on the chemistry of the starting lake (Tosca and Tutolo, 2023). Some studies suggested potential alternative sources of oxidants with bromates to explain the oxidation of Mn (Mitra et al., 2022). Although this experimental study proved that bromates can oxidize Mn at decent rates, and that is a valid mechanism on a local scale, the amount of Br required for such oxidation to occur globally is debated. One common point of the Mn enrichment was that they were found in late stage veins, or alternatively in nodules which might be associated with late stage fluids, demonstrating a relative mobility of Mn. Interestingly, the Fe-Mn-P-Mg-rich “Groken” nodules in the Glen Torridon region also revealed association of P and Fe similar to what we report under acidic conditions (Treiman et al., 2023).

Recently, in the orbitally identified sulfate unit in Gale crater, more evidence of open system alteration and evaporation has been reported. The composition of the Amapari Marker Band showed a very high enrichment in Mn and Fe, implying that they were transported and precipitated in this outcrop (Gasda et al., 2023). Furthermore, the recent detection and inference of chemical sedimentation of siderite by CheMin (Tutolo et al., 2024) showed that Fe was mobile in the alteration fluids.

6.3. Implication for Fe-carbonates on mars

The carbonate conundrum has been under investigation since the early days of Mars' exploration. Multiple explanations have been proposed for the lack of carbonates on Mars. In particular, siderite should be a common carbonate when weathering ferromagnesian rocks under higher $p\text{CO}_2$. We saw in the modeled phase assemblage that siderite (and rhodochrosite in the “H” run) were predicted, but we did not observe any in the phase assemblage. Other alteration experiments with comparable conditions, and despite the higher reactive surface areas, higher temperature, or longer times, did not report clear siderite precipitation either (Bullock et al., 2004; Fabre et al., 2011; Dehouck et al., 2012, 2014a; Viennet et al., 2019; Baron et al., 2019; Gil-Lozano et al., 2024).

Using our kinetic sensitivity test model (Section 6.2), we extracted the total phase assemblage (primary and secondary phases) in each simulation run and calculated the bulk proportion of Fe-oxide and siderite for every time increment: the final time proportions are represented as a heatmap (with intensity of red as Fe-oxide and intensity of green as siderite) on which are overlapped the isochrones corresponding to a given bulk proportion reached in the $p\text{CO}_2/p\text{O}_2$ area at a given time step (Fig. 8). The transition between Fe-oxide and Fe-carbonate is positively correlated between $p\text{CO}_2/p\text{O}_2$ (diagonal boundary between red and green), similarly to the Fe concentration mobility boundary in Fig. 7, where Fe remains more mobile in the predominant siderite area than in the predominant Fe-oxide area at the final time.

The simulations reveal that:

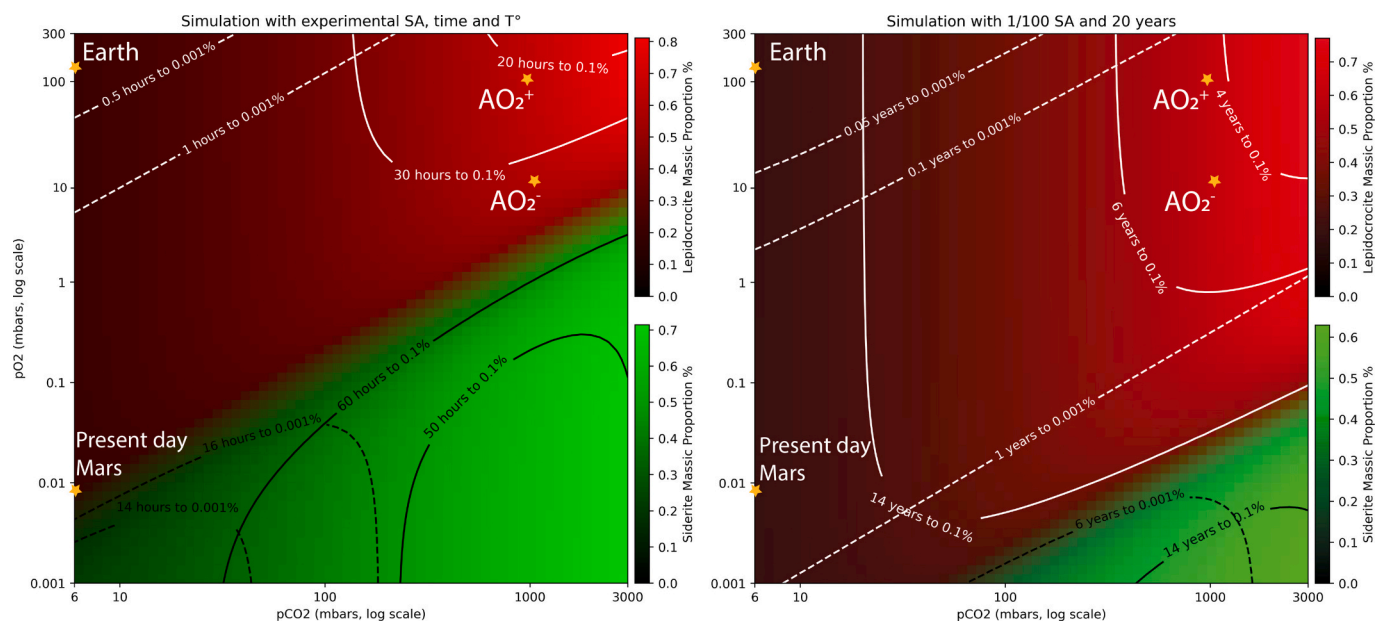


Fig. 8. Sensitivity test of our kinetic alteration model: siderite and Fe-oxide bulk proportion and timing. The heat-map displays siderite and Fe-oxide bulk proportions at the final time, respectively as intensities of green and red. Isochrones are delimiting areas where a given proportion is reached at a given time in the pCO₂/pO₂ space. The transition area between Siderite and Fe-oxides appear as a brownish color when their proportions are equivalent. Yellow stars show the present day Mars and Earth conditions as well as the AO₂⁻ and AO₂⁺ experiments, which now both predict Fe-oxide compared to the initial model in Fig. 6. One may want to link siderite and Fe-oxide precipitation to the fluid concentrations of the Fig. 7, where the heatmap can be visualized as the top plan of the cubes A and C (concentrations at final time across pCO₂ and pO₂) and the isochrones related to variation in concentration through time in these cubes. (For interpretation of the references to color in this figure legend, the reader is referred to the web version of this article.)

1. By placing our experiments on their corresponding pCO₂ and pO₂ simulations (as yellow stars in Fig. 8), we now correctly predict Fe-oxide precipitation for both AO₂⁻ and AO₂⁺ differently from the initial model that predicts only siderite or a mixture of both (Fig. 6). Although we do not have precise oxygen values for other experimental studies to be placed directly on the heatmap, their absence of observed siderite might be explained either by oxygen contamination or by a still insufficient pH and reaction times (see point 3). Present day Mars and Earth are clearly placed in oxidizing, Fe-oxide-producing conditions.
2. Although the final bulk proportions are highest at high pCO₂, precipitation of Fe-oxides or siderite occurs first at the lower part of their pCO₂ precipitation domain (0.001% bulk isochrones in the left side of their color area, Fig. 8) and then transition to higher proportions only after longer times at higher pCO₂ (0.1% bulk isochrones in the right side of their color area, Fig. 8). For Fe-oxides, this shows that initial precipitation is favored by higher pH (enhanced oxidation rates), but higher proportions are produced only when weathering rates are higher (at higher pCO₂) and after longer times (higher buffering). Siderite precipitation also requires higher pH, which is reached faster when pCO₂ is lower, but also only increases in greater proportion with higher pCO₂ and longer times (weathering rates and buffering).
3. The initial precipitation of siderite and oxide is separated by 1 order of magnitude in time, as shown by 0.001% isochrones. For example, in Fig. 8, the isochrones in the heatmap at 1/100 SA and 20 years show that almost all the final Fe-oxide pCO₂ and pO₂ domain have already seen Fe-oxide precipitation after 1 year while 6 years are needed to have precipitation in only a fraction of the siderite domain. At experimental conditions, this separation is even greater with 1 h and 14 h to reach similar fractions in their domains. This is particularly important because it shows that below a certain residence time (buffering, thus activities and pH), only Fe-oxides will be able to form, while siderite will not form under any conditions. This is shown by the concentration peak and decrease in Fe formed by siderite precipitation (for example, in C at pCO₂ = 0.5 and pO₂ = -4,

Fig. 7), which occurs later than the early decrease in Fe concentration at higher pO₂ caused by oxidation (for example, in C at pCO₂ = 0.5 and pO₂ = -2).

In a Martian open system at low residence time, even in the pCO₂/pO₂ domain allowing siderite, it is likely that siderite could not form without later evaporation or higher weathering rates because steady-state pH and alkalinity are too low to effectively trigger its precipitation, as proposed in a previous study (Tosca et al., 2018). The kinetic rates of precipitation of siderite and rhodochrosite are generally much lower than those of calcite, which explains persistent saturation in some terrestrial groundwater (Jensen et al., 2002; Jiang and Tosca, 2020). When the rates are taken into account, they increase the need for higher activities (evaporation or weathering rates) to enhance the precipitation rate by chemical affinity. Other carbonates such as calcite could also be difficult to form; even if its precipitation is favored by higher rates, Mg and Mn-rich fluids could inhibit its precipitation (Mills et al., 2022), and these elements were probably present in the Martian alteration fluid. It is likely why most models based only on equilibrium are overestimating carbonates.

Our kinetic model shows that coprecipitation of oxides and carbonates is possible and can give information on the pH/redox conditions if we assume that their precipitation is not linked to higher weathering rates or evaporation in the first place. In a syndepositional scenario, only finding Fe (and Mn) carbonates would be a clue for a reducing or at least a lower-level oxidizing atmosphere (relative to our simulation). On the other hand, finding a mixture of Fe-carbonates, Fe-oxides, and potentially Mn-carbonates would suggest more moderate oxidizing conditions and a sufficiently high pH. In the same way, a bulk consisting of Fe-oxide and Mn-carbonate would advocate for moderate-high oxidative conditions and higher pH. Recent detection of Fe-carbonates in the Chenapau Member of the Mirador Formation (also known as “sulfates unit” from orbital data) (Tutolo et al., 2024) as well as the strong enrichment of Mn and Fe in the Amapari Marker Band (Gasda et al., 2023) could be used to determine the water composition required and the redox / pH associated

with a change in hydrology (evaporation, higher weathering rates, briny groundwater rising) and as a proxy for atmospheric composition. On the one hand, considering the slow kinetic rate of precipitation of Mn-carbonate, its presence would require that all Fe-oxides sorption sites would be saturated or passivated to prevent catalysis or that leaching effectively separates Mn-rich water from Fe-oxides. Mn could also be integrated in the siderite if collocated precipitation occurs, as it partitions strongly and could yield a significant amount of Mn in the mineral even with a relatively low Mn concentration in the fluid (Sengupta et al., 2020).

6.4. Limits and improvements of the model with the experimental feedback

We reported several discrepancies between the model and the data: 1- Overestimation/Underestimation of concentration and buffering. 2- Overestimation of the precipitation of secondary phases, in particular siderite and clays. These two points are linked, depending on the conditions.

On the first point, the Mn concentration overestimation (in runs starting with pure water) is most likely explained by the absence of one or several mechanisms in the model (catalysis and/or adsorption). Alternatively, it is possible that one or several Mn-bearing phases are lacking in the database and precipitate in quantities that did not allow their observation. There can be multiple reasons for the overestimation of [Fe]: reactive surfaces (SA), discrepancies in rate constants caused by equilibrium interfaces at the mineral surfaces, or discrepancies on the measured rate constants far from equilibrium, especially in witness experiments.

Regarding SA, we preferred to test our method of theoretical SA calculation over the BET surface area. However, SA is often treated as a fitting parameter to achieve good agreement with the experimental results, with uncertainties up to one order of magnitude between BET derived surface and geometrical surface or even higher for clay minerals (Bourg et al., 2015). Concentrations and buffering speeds will change with an increase or decrease of the total SA, or a wrong estimation of mineral specific reactive area (Beckingham et al., 2016). However, in a Martian approach, fitting by adjusting the SA of each minerals would be beyond the scope of the paper as we do not have water chemistry compositions.

Discrepancies between field data (or here a real rock dissolution) and models are observed in multiple studies and can be attributed to the incomplete description of the complex interaction between dissolution and precipitation, as well as the methods of how far from equilibrium kinetic rate constants are measured (Zhu and Lu, 2013). Temperature dependencies of dissolution rates also seems to be overestimated, as shown in the runs at high temperature starting with pure water. Moreover, temperature dependencies for oxidation rates remain unknown, so we can expect an effective change in rates when conditions are far from the standard temperature. Additionally, the grain-water interface can locally reach an equilibrium concentration, effectively limiting dissolution rates. Our daily agitation was purposely done to avoid this effect without speeding up the dissolution rates. When the rates are measured, the effective rates are most often faster because the mixing method is optimal, with continuous stirring throughout the experiments. When calculating our solid solution, we also made the assumption of a proportional change of rates between the end-members, which could favor faster dissolution when some end-members have several orders of magnitudes between their rate constants (Lichtner, 2016). Passivation of the mineral surface was also proposed in previous experiments to explain the lower pH.

Most of the overestimation of precipitation is related to point 1: Increased activities and pH favor the precipitation of secondary phases. Moreover, specific to the overestimated clay production, their precipitation kinetics are several orders of magnitude slower than other phases such as carbonates or oxides (Meunier, 2005; Marty et al., 2015).

Combined with their extremely favored precipitation in thermodynamic models because of their low solubility, their overestimated production can be explained quite straightforwardly. With respect to siderite, it is clear that its precipitation is limited by the level of supersaturation needed for precipitation (Tosca et al., 2018). Supersaturation that allows siderite precipitation is harder to reach than for Fe-oxide as shown in Section 6.3. On the ancient Mars surface, it could be more challenging to form because the pH/alkalinity domain is most of the time incompatible when being at high W/R and in direct contact with the atmosphere.

To address these precipitation overestimations, future models must include a more accurate description of siderite precipitation that takes into account the effective supersaturation needed to precipitate and, if possible, their precipitation kinetics. Clay precipitation will be hindered by its precipitation rates, so it is best to include them when available. Without precipitation kinetics, removal of clays from the model, in the context of a short-lived environment, similar to our sensitivity simulation, would give the best results.

Further sensitivity tests could include a larger change in SA to constrain the wider predominance domain of siderite and Fe-oxide while staying in a geologically realistic setting. Even if it would not be a first order controlling factor for Fe and Mn, testing multiple starting rocks with extreme composition differences (such as dunite vs. anorthosite) could be interesting to test out the effect on secondary phase precipitation. In the future, with the available range of possible minerals in our thermo-kinetic calculator, and pending a direct interface with the PhreeqPy simulation, it would be possible to quickly compute the full range of rock composition from ultramafic to acid series and perform kinetic dissolution calculations. It would also be possible to explore the effect of the variation of the solid solution composition of minerals on the fluid evolution and the predicted phase mixture.

Furthermore, it was observed that certain mechanisms may not be included in the model. Therefore, incorporating adsorption or catalysis, where applicable and feasible, could be crucial as they may significantly influence the concentrations of certain elements.

The assumption of congruent dissolution of the solid solution including Mn seems mostly correct, since the concentrations are correctly predicted in acid runs dominated by the dissolution. It would be possible to include other minor substituents in the primary silicate solution.

7. Conclusion

The kinetic weathering experiments conducted in this study once more emphasizes the importance of kinetics when trying to interpret redox and paleoenvironmental conditions based on the final phase assemblage found in-situ. These experiments showed that the evolution of Fe and Mn concentrations in the fluid is complex and mostly controlled by kinetics. Overall, the runs with different pO₂ did not result in a significant change in the mineralogy, because more than an order of magnitude of difference in pO₂ and/or higher alkalinity would be required, as modeled in our simulation with updated parameters. On the other hand, thanks to the experimental “sensitivity test” approach, we compared multiple parameters in order to decipher the controlling factors in a whole rock alteration experiment. In the runs starting with pure water, we observed that, despite an apparent stabilization of fluid chemistry, the final Fe concentration was, in fact, controlled by a “dynamic” or steady-state equilibrium between dissolution and oxidation rates. Moreover, Mn concentration, while much higher than predicted by the equilibrium-based model, was likely controlled by one or several mechanisms related to Fe-oxide formation. Therefore, its apparent final equilibrium was probably controlled by the dynamic equilibrium between the dissolution rates and these unidentified mechanisms (possibly catalysis, adsorption, and/or Fe-Mn-bearing phase precipitation). On Mars, it is hence most probable that Mn and Fe might be associated because of this process, while Mn could stay relatively mobile even where a significant amount of Fe-oxide forms. Moreover, if we

hypothesize that Fe-oxides are not available, Mn would be even more mobile, as predicted by the “kdtp” model.

In the runs starting with acidic solutions, we saw that the main control over the solution composition was the dissolution kinetics, even in the stable pseudo-equilibrium phase. Although it has no apparent impact on the Fe concentration, we also observed in these runs the precipitation of a secondary phase composed of Fe, S and P. While apatite was only a minor fraction of the initial phase assemblage, the presence of P in the phase assemblage was enhanced because of its faster dissolution kinetics. If the models manage to predict a satisfying description of the evolution of concentration and of the final pseudo-equilibrium, we show that they often overestimated the precipitation of secondary phases such as clays and siderite. A part of the explanation for these discrepancies was the absence of precipitation kinetics for clays and because of the actual supersaturation needed to effectively precipitate siderite.

Based on these experimental observations, we updated the model with a higher supersaturation required for siderite precipitation and removed clays from the potential phases that can precipitate. We conducted a large kinetic sensitivity test simulation which confirmed the absence of siderite in our experimental conditions. We were able to determine that even under oxidizing conditions from a thermodynamic standpoint, it is possible to form siderite. Going beyond equilibrium models, we calculated a new pO_2 and pCO_2 space where siderite or Fe-oxide can be effectively formed, redefining the meaning of “reducing” and “oxidizing” in a Martian context. Moreover, we also observed that without longer residence time, the Fe activity and pH are not compatible with the formation of siderite under any conditions. Observing siderite or oxide would not primarily be a redox marker but would be a clue for a different hydrological regime. Based on these results, we interpret that formation of Fe–Mg and Fe carbonates, such as is observed by the Perseverance rover in Jezero crater or by the Curiosity rover in Gale crater, would not be a marker of a particularly reducing atmosphere, but instead as an indicator of changing hydrological conditions that result in high alkalinity and/or higher pH. Although siderite would not infer primarily redox conditions, and that Mn-oxides are mainly pH controlled and do not require terrestrial-level amounts of oxygen, a collocated precipitation of siderite and Mn-oxides could still provide valuable information to constrain the redox environment of the ancient Mars. At a global scale, the formation of authigenic siderite and even other carbonates (for example, when accounting the Mg-inhibition of calcite precipitation) during rock weathering would be rather limited without long residence times. It can be interpreted that higher weathering rates and buffering during alteration or ultimately later evaporation are required to form siderite on the surface of Mars.

Both Fe and Mn would have greatly enhanced mobility on the Martian surface. Relatively high pO_2 and low pCO_2 combined with a longer residence time in the water would be the only way to have a reduced mobility of Fe, while still being much higher than on Earth. Close or collocated precipitation of oxide and carbonates would be possible without a change in the pO_2 content of the atmosphere within the same oxidation front. This new quantification of kinetic-induced mobility of Fe and Mn can serve to update existing and future hypotheses on the redox and paleo-environmental significance of their associated secondary phases when found in-situ on Mars.

CRediT authorship contribution statement

Matteo Loche: Writing – original draft, Visualization, Supervision, Software, Resources, Project administration, Methodology, Investigation, Formal analysis, Conceptualization. **Sébastien Fabre:** Writing – review & editing, Validation, Supervision, Software, Project administration, Methodology, Investigation, Conceptualization. **Agnès Cousin:** Writing – review & editing, Supervision, Project administration, Investigation, Funding acquisition. **Arnaud Proietti:** Writing – review & editing, Methodology, Investigation, Conceptualization. **William**

Rapin: Writing – review & editing, Conceptualization. **Benjamin M. Tutolo:** Writing – review & editing. **Pierre-Yves Meslin:** Writing – review & editing, Validation, Conceptualization. **Anissa Benmammar:** Methodology, Resources, Validation. **Foteine Dimitracopoulos:** Writing – review & editing. **Roger C. Wiens:** Writing – review & editing, Funding acquisition. **Olivier Gasnault:** Writing – review & editing, Funding acquisition.

Declaration of competing interest

The authors declare that they have no known competing financial interests or personal relationships that could have appeared to influence the work reported in this paper.

Data availability

Data will be made available on request.

Acknowledgements

The authors are grateful to the MSL and M2020 teams for their scientific advice and support. We also thank CNES in France and the funding in the US provided by NASA's Mars Exploration Program that enabled this research. I personally thank D.Parkhurst for the help provided over the years for the PHREEQC community, and in particular for his corrections on our kinetic code. I thank Anissa Benmammar for the hard work of sampling several lava flows for us. I thank Arnaud Proietti for his valuable help and quality data for the EBSD. I also thank my former intern Cassandre Chaudesaygues, who worked on the experimental data. I thanks Aurélien Paulmier for allowing us to use his oxygen sensor.

Appendix A. Supplementary data

Supplementary data to this article can be found online at <https://doi.org/10.1016/j.chemgeo.2024.122242>.

References

- Albert, S., Flores, O., Michon, L., Strasberg, D., 2020. Dating young (! 1000 yr) lava flow eruptions of piton de la fournaise volcano from size distribution of long-lived pioneer trees. *J. Volcanol. Geotherm. Res.* 401, 106974.
- Anbar, A., Holland, H., 1992. The photochemistry of manganese and the origin of banded iron formations. *Geochim. Cosmochim. Acta* 56, 2595–2603. URL: <https://linkinghub.elsevier.com/retrieve/pii/001670379290346K> [https://doi.org/10.1016/0016-7037\(92\)90346-K](https://doi.org/10.1016/0016-7037(92)90346-K).
- Baron, F., Gaudin, A., Lorand, J., Mangold, N., 2019. New constraints on early mars weathering conditions from an experimental approach on crust simulants. *J. Geophys. Res. Planets* 124, 1783–1801. URL: <https://onlinelibrary.wiley.com/doi/10.1029/2019JE005920> <https://doi.org/10.1029/2019JE005920>.
- Beckingham, L.E., Mitnick, E.H., Steefel, C.I., Zhang, S., Voltolini, M., Swift, A.M., Yang, L., Cole, D.R., Sheets, J.M., Ajo-Franklin, J.B., DePaolo, D.J., Mito, S., Xue, Z., 2016. Evaluation of mineral reactive surface area estimates for prediction of reactivity of a multi-mineral sediment. *Geochim. Cosmochim. Acta* 188, 310–329. URL: <https://linkinghub.elsevier.com/retrieve/pii/S0016703716303003> <https://doi.org/10.1016/j.gca.2016.05.040>.
- Bedford, C., Bridges, J., Schwenzer, S., Wiens, R., Rampe, E., Frydenvang, J., Gasda, P., 2019. Alteration trends and geochemical source region characteristics preserved in the fluviolacustrine sedimentary record of Gale crater, Mars. *Geochim. Cosmochim. Acta* 246, 234–266. URL: <https://linkinghub.elsevier.com/retrieve/pii/S0016703718306616> <https://doi.org/10.1016/j.gca.2018.11.031>.
- Berger, J.A., King, P.L., Gellert, R., Clark, B.C., Flood, V.A., McCraig, M.A., Ming, D.W., O'Connell-Cooper, C.D., Schmidt, M.E., Thompson, L.M., VanBommel, S.J.V., Wilhelm, B., Yen, A.S., 2022. Manganese Mobility in Gale Crater, Mars: Leached Bedrock and Localized Enrichments. *J. Geophys. Res. Planets* 127. URL: <https://onlinelibrary.wiley.com/doi/10.1029/2021JE007171>, doi:<https://doi.org/10.1029/2021JE007171>.
- Bishop, J.L., Fairén, A.G., Michalski, J.R., Gago-Duport, L., Baker, L.L., Velbel, M.A., Gross, C., Rampe, E.B., 2018. Surface clay formation during short-term warmer and wetter conditions on a largely cold ancient Mars. *Nature. Astronomy* 2, 206–213.

- URL: <http://www.nature.com/articles/s41550-017-0377-9> <https://doi.org/10.1038/s41550-017-0377-9>.
- Blake, D.F., Morris, R.V., Kocurek, G., Morrison, S.M., Downs, R.T., Bish, D., Ming, D.W., Edgett, K.S., Rubin, D., Goetz, W., Madsen, M.B., Sullivan, R., Gellert, R., Campbell, I., Treiman, A.H., McLennan, S.M., Yen, A.S., Grotzinger, J., Vaniman, D. T., Chipera, S.J., Achilles, C.N., Rampe, E.B., Sumner, D., Meslin, P.Y., Maurice, S., Forni, O., Gasnault, O., Fisk, M., Schmidt, M., Mahaffy, P., Leshin, L.A., Glavin, D., Steele, A., Freissinet, C., Navarro-González, R., Yingst, R.A., Kah, L.C., Bridges, N., Lewis, K.W., Bristow, T.F., Farmer, J.D., Crisp, J.A., Stolper, E.M., Des Marais, D.J., Sarrazin, P., Science Team, M.S.L., Agard, C., Alves Verdasca, J.A., Anderson, R., Anderson, R., Archer, D., Armiens-Aparicio, C., Arvidson, R., Atkinson, E., Atreya, S., Aubrey, A., Baker, B., Baker, M., Balic-Zunic, T., Baratoux, D., Barouk, J., Barraclough, B., Bean, K., Beegle, L., Behar, A., Bell, J., Bender, S., Benna, M., Bentz, J., Berger, G., Berger, J., Berman, D., Blanco Avalos, J.J., Blaney, D., Blank, J., Blau, H., Bleacher, L., Boehm, E., Botta, O., Böttcher, S., Boucher, T., Bower, H., Boyd, N., Boynton, B., Breves, E., Bridges, J., Brinckerhoff, W., Brinza, D., Brunet, C., Brunner, A., Brunner, W., Buch, A., Bullock, M., Burmeister, S., Cabane, M., Calef, F., Cameron, J., Cantor, B., Caplinger, M., Rodríguez, J.C., Carmosino, M., Blázquez, I. C., Charpentier, A., Choi, D., Clark, B., Clegg, S., Cleghorn, T., Cloutis, E., Cody, G., Coll, P., Conrad, P., Coscia, D., Cousin, A., Cremers, D., Cros, A., Cucinotta, F., d'Uston, C., Davis, S., Day, M., Juárez, M.D.L.T., DeFlores, L., DeLapp, D., DeMarines, J., Dietrich, W., Dingler, R., Donny, C., Drake, D., Dromart, G., Dupont, A., Duston, B., Dworkin, J., Dyar, M.D., Edgar, L., Edwards, C., Edwards, L., Ehlmann, B., Ehresmann, B., Eigenbrode, J., Elliott, B., Elliott, H., Ewing, R., Fabre, C., Fairén, A., Farley, K., Fassett, C., Favot, L., Fay, D., Fedosov, F., Feldman, J., Feldman, S., Fitzgibbon, M., Fleisch, G., Floyd, M., Flückiger, L., Fraeman, A., Francis, R., François, P., Franz, H., French, K.L., Frydenvang, J., Gaboriaud, A., Gailhanou, M., Garvin, J., Geoffroy, C., Genzer, M., Godber, A., Goesmann, F., Golovin, D., Gómez, F.G., Gómez-Elvira, J., Gondet, B., Gordon, S., Gorevan, S., Grant, J., Griffes, J., Grinspoon, D., Guillemot, P., Guo, J., Gupta, S., Guzewich, S., Haberle, R., Halleaux, D., Hallet, B., Hamilton, V., Hardgrove, C., Harker, D., Harpold, D., Harri, A.M., Harshman, K., Hassler, D., Haukka, H., Hayes, A., Herkenhoff, K., Herrera, P., Hettrich, S., Heydari, E., Hipkin, V., Hoehler, T., Hollingsworth, J., Hudgins, J., Huntress, W., Hurowitz, J., Hviid, S., Iagnemma, K., Indyk, S., Israël, G., Jackson, R., Jacob, S., Jakosky, B., Jensen, E., Jensen, J.K., Johnson, J., Johnson, M., Johnstone, S., Jones, A., Jones, J., Joseph, J., Jun, I., Kahanpää, H., Kahre, M., Karpushkina, N., Kasprzak, W., Kauhanen, J., Keely, L., Kemppinen, O., Keymeulen, D., Kim, M.H., Kinch, K., King, P., Kirkland, L., Koefoed, A., Köhler, J., Kortmann, O., Kozayev, A., Krezoski, J., Kryasov, D., Kuzmin, R., Lacour, J.L., Lafaillle, V., Langevin, Y., Lanza, N., Lasue, J., Le Mouélic, S., Lee, E.M., Lee, Q.M., Lees, D., Lefavor, M., Lemmon, M., Lepinette Malvitte, A., Léveillé, R., Lewin-Carpentier, E., Li, S., Lipkaman, L., Little, C., Litvak, M., Lorigny, E., Lugmair, G., Lundberg, A., Lyness, E., Maki, J., Malakhov, A., Malespín, C., Malin, M., Mangold, N., Manning, H., Marchand, G., Marín Jiménez, M., Martín García, C., Martín, D., Martín, M., Martínez-Frías, J., Martín-Soler, J., Martín-Torres, F.J., Mauchien, P., McAdam, A., McCartney, E., McConnochie, T., McCullough, E., McEwan, I., McKay, C., McNair, S., Melikechi, N., Meyer, M., Mezzacappa, A., Miller, H., Miller, K., Milliken, R., Minitti, M., Mischna, M., Mitrofanov, I., Moersch, J., Mokrousov, M., Molina Jurado, A., Moores, J., Mora-Sotomayor, L., Morookian, J.M., Mueller-Mellin, R., Müller, J.P., Muñoz Caro, G., Nachon, M., Navarro López, S., Nealson, K., Nefian, A., Nelson, T., Newcombe, M., Newman, C., Newsom, H., Nikiforov, S., Niles, P., Nixon, B., Dobreá, E.N., Nolan, T., Oehler, D., Ollila, A., Olson, T., Owen, T., Pablo, H., Paillet, A., Pallier, E., Palucis, M., Parker, T., Parot, Y., Patel, K., Paton, M., Paulsen, G., Pavlov, A., Pavri, B., Peinado-González, V., Pepin, R., Peret, L., Perez, R., Perrett, G., Peterson, J., Pílorget, C., Pinet, P., Pla-García, J., Plante, I., Poitras, F., Polkko, J., Popp, R., Posiolova, L., Pradler, I., Prats, B., Prokhorov, V., Purdy, S.W., Raean, E., Radziemski, L., Rafkin, S., Ramos, M., Raulin, F., Ravine, M., Reitz, G., Rennó, N., Rice, M., Richardson, M., Robert, F., Rodríguez Manfredi, J.A., Romeral-Planelló, J.J., Rowland, S., Saccoccio, M., Salamon, A., Sandoval, J., Sanin, A., Sans Fuentes, S.A., Saper, L., Sautter, V., Savijärvi, H., Schieber, J., Schmidt, W., Scholtes, D., Schoppers, M., Schröder, S., Sebastian Martínez, E., Sengstacken, A., Shterts, R., Siebach, K., Silli, T., Simmonds, J., Sirven, J.B., Slavney, S., Sletten, R., Smith, M., Sobrón Sánchez, P., Spanovich, N., Spray, J., Squyres, S., Stack, K., Stalport, F., Stein, T., Stern, J., Stewart, N., Stipp, S.L.S., Stoiber, K., Sucharski, B., Summons, R., Sun, V., Supulver, K., Sutter, B., Szopa, C., Tate, C., Teinturier, S., ten Kate, I.L., Thomas, P., Thompson, L., Tokar, R., Toplis, M., Torres Redondo, J., Trainer, M., Tretyakov, V., Urqui-O'Callaghan, R., Van Beek, J., Van Beek, T., VanBommel, S., Varenikov, A., Vasavada, A., Vasconcelos, P., Vicenzi, E., Vostrukhin, A., Voytek, M., Wadhwa, M., Ward, J., Webster, C., Weigle, E., Wellington, D., Westall, F., Wiens, R.C., Wilhelm, M.B., Williams, A., Williams, J., Williams, R., Williams, R.B., Wilson, M., Wimmer-Schweingruber, R., Wolff, M., Wong, M., Wray, J., Wu, M., Yana, C., Zeitlin, C., Zimdar, R., Zorzano Mier, M.P., 2013. Curiosity at Gale Crater, Mars: characterization and analysis of the rocknest sand shadow. *Science* 341, 1239505. URL: <https://www.science.org/doi/10.1126/science.1239505> <https://doi.org/10.1126/science.1239505>.
- Blanc, P., Lassin, A., Piantone, P., Azaroual, M., Jacquemet, N., Fabbri, A., Gaucher, E., 2012. Thermoddb: A geochemical database focused on low temperature water/rock interactions and waste materials. *Appl. Geochem.* 27, 2107–2116. URL: <https://linkinghub.elsevier.com/retrieve/pii/S0883292712001497> <https://doi.org/10.1016/j.apgeochem.2012.06.002>.
- Borlina, C.S., Ehlmann, B.L., Kite, E.S., 2015. Modeling the thermal and physical evolution of Mount Sharp's sedimentary rocks, Gale Crater, Mars: Implications for diagenesis on the MSL Curiosity rover traverse. *J. Geophys. Res. Planets* 120, 1396–1414. URL: <https://onlinelibrary.wiley.com/doi/10.1002/2015JE004799> <https://doi.org/10.1002/2015JE004799>.
- Bourg, I.C., Beckingham, L.E., DePaolo, D.J., 2015. The nanoscale basis of CO₂ trapping for geologic storage. *Environ. Sci. Technol.* 49, 10265–10284.
- Bristow, T.F., Haberle, R.M., Blake, D.F., Des Marais, D.J., Eigenbrode, J.L., Fairén, A.G., Grotzinger, J.P., Stack, K.M., Mischna, M.A., Rampe, E.B., Siebach, K.L., Sutter, B., Vaniman, D.T., Vasavada, A.R., 2017. Low Hesperian PCO₂ constrained from in situ mineralogical analysis at Gale Crater, Mars. *Proc. Natl. Acad. Sci.* 114, 2166–2170. URL: <http://www.pnas.org/lookup/doi/10.1073/pnas.1616649114> <https://doi.org/10.1073/pnas.1616649114>.
- Bristow, T., Grotzinger, J.P., Rampe, E., Cuadros, J., Chipera, S., Downs, G., Fedo, C.M., Frydenvang, J., McAdam, A., Morris, R., et al., 2021. Brine-driven destruction of clay minerals in gale crater, mars. *Science* 373, 198–204.
- Bullock, M.A., Moore, J.M., Mellon, M.T., 2004. Laboratory simulations of Mars aqueous geochemistry. *Icarus* 170, 404–423. URL: <https://linkinghub.elsevier.com/retrieve/pii/S0019103504001228> <https://doi.org/10.1016/j.icarus.2004.03.016>.
- Carter, J., Poulet, F., Bibring, J.P., Mangold, N., Murchie, S., 2013. Hydrous minerals on Mars as seen by the crism and omega imaging spectrometers: Updated global view. *J. Geophys. Res. Planets* 118, 831–858.
- Charlton, S.R., Parkhurst, D.L., 2011. Modules based on the geochemical model PHREEQC for use in scripting and programming languages. *Comput. Geosci.* 37, 1653–1663. URL: <https://doi.org/10.1016/j.cageo.2011.02.005>.
- Clavé, E., Benzerara, K., Meslin, P., Forni, O., Royer, C., Mandon, L., Beck, P., Quantin-Nataf, C., Beyssac, O., Cousin, A., Bousquet, B., Wiens, R., Maurice, S., Dehouck, E., Schröder, S., Gasnault, O., Mangold, N., Dromart, G., Bosak, T., Bernard, S., Udry, A., Anderson, R., Arana, G., Brown, A., Castro, K., Clegg, S., Cloutis, E., Fairén, A., Flannery, D., Gasda, P., Johnson, J., Lasue, J., Lopez-Reyes, G., Madariaga, J., Manrique, J., Le Mouélic, S., Núñez, J., Ollila, A., Pilleri, P., Pilorget, C., Pinet, P., Poulet, F., Veneranda, M., Wolf, Z., the SuperCam team, 2022. Carbonate detection with SuperCam in igneous rocks on the floor of Jezero Crater, Mars. *J. Geophys. Res. Planets.* <https://doi.org/10.1029/2022JE007463>.
- David, G., Cousin, A., Forni, O., Meslin, P.Y., Dehouck, E., Mangold, N., L'Haridon, J., Rapin, W., Gasnault, O., Johnson, J., et al., 2020. Analyses of high-iron sedimentary bedrock and diagenetic features observed with chemcam at vera rubin ridge, gale crater, mars: calibration and characterization. *J. Geophys. Res. Planets* 125, e2019JE006314.
- Dehouck, E., Chevrier, V., Gaudin, A., Mangold, N., Mathé, P.E., Rochette, P., 2012. Evaluating the role of sulfide-weathering in the formation of sulfates or carbonates on Mars. *Geochim. Cosmochim. Acta* 90, 47–63. URL: <https://linkinghub.elsevier.com/retrieve/pii/S0016703712002736> <https://doi.org/10.1016/j.gca.2012.04.057>.
- Dehouck, E., Gaudin, A., Mangold, N., Lajaunie, L., Dauzères, A., Grauby, O., Le Menn, E., 2014a. Weathering of olivine under CO₂ atmosphere: A martian perspective. *Geochim. Cosmochim. Acta* 135, 170–189. URL: <https://linkinghub.elsevier.com/retrieve/pii/S0016703714002117> <https://doi.org/10.1016/j.gca.2014.03.032>.
- Dehouck, E., Gaudin, A., Mangold, N., Lajaunie, L., Dauzères, A., Grauby, O., Le Menn, E., 2014b. Weathering of olivine under CO₂ atmosphere: A martian perspective. *Geochim. Cosmochim. Acta* 135, 170–189. URL: <https://linkinghub.elsevier.com/retrieve/pii/S0016703714002117> <https://doi.org/10.1016/j.gca.2014.03.032>.
- Dehouck, E., Gaudin, A., Chevrier, V., Mangold, N., 2016. Mineralogical record of the redox conditions on early Mars. *Icarus* 271, 67–75. URL: <https://linkinghub.elsevier.com/retrieve/pii/S001910351600052X> <https://doi.org/10.1016/j.icarus.2016.01.030>.
- Drouet, C., Loche, M., Fabre, S., Meslin, P., 2021. On the occurrence of Jahnite/Whiteite phases on Mars: a thermodynamic study. *Am. Mineral.* <https://doi.org/10.2138/am-2022-8174>.
- Ehlmann, B.L., Mustard, J.F., Fassett, C.I., Schon, S.C., Head III, J.W., Des Marais, D.J., Grant, J.A., Murchie, S.L., 2008. Clay minerals in delta deposits and organic preservation potential on Mars. *Nat. Geosci.* 1, 355–358.
- Fabre, S., Berger, G., Nédélec, A., 2011. Modeling of continental weathering under high-CO₂ atmospheres during Precambrian times: CONTINENTAL WEATHERING DURING PCB TIMES. *Geochem. Geophys. Geosyst.* 12 <https://doi.org/10.1029/2010GC003444> n/a–n/a.
- Fairén, A.G., Davila, A.F., Gago-Duport, L., Haqq-Misra, J.D., Gil, C., McKay, C.P., Kasting, J.F., 2011. Cold glacial oceans would have inhibited phyllosilicate sedimentation on early Mars. *Nat. Geosci.* 4, 667–670. URL: <http://www.nature.com/articles/ngeo1243> <https://doi.org/10.1038/ngeo1243>.
- Fairén, A.G., Gil-Lozano, C., Uceda, E.R., Losa-Adams, E., Davila, A.F., Gago-Duport, L., 2017. Mineral paragenesis on Mars: the roles of reactive surface area and diffusion. *J. Geophys. Res. Planets* 122, 1855–1879.
- Farley, K.A., Stack, K.M., Shuster, D.L., Horgan, B.H.N., Hurowitz, J.A., Tarnas, J.D., Simon, J.I., Sun, V.Z., Scheller, E.L., Moore, K.R., McLennan, S.M., Vasconcelos, P. M., Wiens, R.C., Treiman, A.H., Mayhew, L.E., Beyssac, O., Kizovski, T.V., Tosca, N. J., Williford, K.H., Crumpler, L.S., Beegle, L.W., Bell, J.F., Ehlmann, B.L., Liu, Y., Maki, J.N., Schmidt, M.E., Allwood, A.C., Amundsen, H.E.F., Bhartiya, R., Bosak, T., Brown, A.J., Clark, B.C., Cousin, A., Forni, O., Gabriel, T.S.J., Goreva, Y., Gupta, S., Hamran, S.E., Herd, C.D.K., Hickman-Lewis, K., Johnson, J.R., Kah, L.C., Kelemen, P. B., Kinch, K.B., Mandon, L., Mangold, N., Quantin-Nataf, C., Rice, M.S., Russell, P.S., Sharma, S., Siljeström, S., Steele, A., Sullivan, R., Wadhwa, M., Weiss, B.P., Williams, A.J., Wogland, B.V., Willis, P.A., Acosta-Maeda, T.A., Beck, P., Benzerara, K., Bernard, S., Burton, A.S., Cardarelli, E.L., Chide, B., Clavé, E.,

- Cloutis, E.A., Cohen, B.A., Czaja, A.D., Debaille, V., Dehouck, E., Fairén, A.G., Flannery, D.T., Fleron, S.Z., Fouchet, T., Frydenvang, J., Garczynski, B.J., Gibbons, E.F., Hausrath, E.M., Hayes, A.G., Henneke, J., Jørgensen, J.L., Kelly, E.M., Lasue, J., Le Mouélic, S., Madariaga, J.M., Maurice, S., Merusi, M., Meslin, P.Y., Milkovich, S.M., Million, C.C., Moeller, R.C., Núñez, J.I., Ollila, A.M., Paar, G., Paige, D.A., Pedersen, D.A.K., Pilleri, P., Pilorget, C., Pinet, P.C., Rice, J.W., Royer, C., Sautter, V., Schulte, M., Sephton, M.A., Sharma, S.K., Sholes, S.F., Spanovich, N., St. Clair, M., Tate, C.D., Uckert, K., VanBommel, S.J., Yanchilina, A. G., Zorzano, M.P., 2022. Aqueously altered igneous rocks sampled on the floor of Jezero crater, Mars. *Science* eabo2196. <https://doi.org/10.1126/science.abo2196>.
- Forni, O., Gaft, M., Toplis, M.J., Clegg, S.M., Maurice, S., Wiens, R.C., Mangold, N., Gasnault, O., Sautter, V., Le Mouélic, S., et al., 2015. First detection of fluorine on Mars: Implications for gale crater's geochemistry. *Geophys. Res. Lett.* 42, 1020–1028.
- Frydenvang, J., Mangold, N., Wiens, R.C., Fraeman, A.A., Edgar, L.A., Fedo, C.M., L'Haridon, J., Bedford, C.C., Gupta, S., Grotzinger, J.P., et al., 2020. The chemostratigraphy of the Murray formation and role of diagenesis at vera rubin ridge in gale crater, mars, as observed by the chemcam instrument. *J. Geophys. Res. Planets* 125, e2019JE006320.
- Gasda, P.J., Haldeman, E.B., Wiens, R.C., Rapin, W., Bristow, T.F., Bridges, J.C., Schwenzner, S.P., Clark, B., Herkenhoff, K., Frydenvang, J., et al., 2017. In situ detection of boron by chemcam on Mars. *Geophys. Res. Lett.* 44, 8739–8748.
- Gasda, P., Lanza, N., Rapin, W., Frydenvang, J., Goetz, W., Schwenzner, S., Dietrich, W., Weitz, C., Bryk, A., Kite, E., et al., 2023. Chemcam observations of the marker band, gale crater, mars. In: 54th Lunar and Planetary Science Conference, p. 2389.
- Gaudin, A., Dehouck, E., Grauby, O., Mangold, N., 2018. Formation of clay minerals on Mars: Insights from long-term experimental weathering of olivine. *Icarus* 311, 210–223. URL: <https://linkinghub.elsevier.com/retrieve/pii/S0019103517306760> <https://doi.org/10.1016/j.icarus.2018.01.029>.
- Gil-Lozano, C., Baron, F., Gaudin, A., Lorand, J.P., Fernandez, V., Hamon, J., Mangold, N., 2024. The key role of bedrock composition in the formation of carbonates on Mars. *Geochim. Perspect. Lett.* 28, 54–59.
- Goddéris, Y., François, L.M., Probst, A., Schott, J., Moncoulon, D., Labat, D., Viville, D., 2006. Modelling weathering processes at the catchment scale: the WITCH numerical model. *Geochim. Cosmochim. Acta* 70, 1128–1147. URL: <https://linkinghub.elsevier.com/retrieve/pii/S0016703705008690> <https://doi.org/10.1016/j.gca.2005.11.018>.
- Grotzinger, J.P., Sumner, D.Y., Kah, L.C., Stack, K., Gupta, S., Edgar, L., Rubin, D., Lewis, K., Schieber, J., Mangold, N., Milliken, R., Conrad, P.G., DesMarais, D., Farmer, J., Siebach, K., Calef, F., Hurowitz, J., McLennan, S.M., Ming, D., Vaniman, D., Crisp, J., Vasavada, A., Edgett, K.S., Malin, M., Blake, D., Gellert, R., Mahaffy, P., Wiens, R.C., Maurice, S., Grant, J.A., Wilson, S., Anderson, R.C., Beegle, L., Arvidson, R., Hallet, B., Sletten, R.S., Rice, M., Bell, J., Griffes, J., Ehlmann, B., Anderson, R.B., Bristow, T.F., Dietrich, W.E., Dromart, G., Eigenbrode, J., Fraeman, A., Hardgrove, C., Herkenhoff, K., Jandura, L., Kocurek, G., Lee, S., Leshin, L.A., Leveille, R., Limonadi, D., Maki, J., McCloskey, S., Meyer, M., Minitti, M., Newsom, H., Oehler, D., Okon, A., Palucis, M., Parker, T., Rowland, S., Schmidt, M., Squyres, S., Steele, A., Stolper, E., Summons, R., Treiman, A., Williams, R., Yingst, A., Team, M.S., Kempainen, O., Bridges, N., Johnson, J.R., Cremers, D., Godber, A., Wadhwa, M., Wellington, D., McEwan, I., Newman, C., Richardson, M., Charpentier, A., Peret, L., King, P., Blank, J., Weigle, G., Li, S., Robertson, K., Sun, V., Baker, M., Edwards, C., Farley, K., Miller, H., Newcombe, M., Pilorget, C., Brunet, C., Hipkin, V., Leveille, R., Marchand, G., Sanchez, P.S., Favot, L., Cody, G., Fluckiger, L., Lees, D., Nefian, A., Martin, M., Gailhanou, M., Westall, F., Israel, G., Agard, C., Barouk, J., Donny, C., Gaboriaud, A., Guillemot, P., Lafaillle, V., Lorigny, E., Paillet, A., Perez, R., Saccoccio, M., Yana, C., Armien-Aparicio, C., Rodriguez, J.C., Blazquez, I.C., Gomez, F.G., Gomez-Elvira, J., Hettrich, S., Malville, A.L., Jimenez, M.M., Martinez-Frias, J., Martin-Soler, J., Martin-Torres, F.J., Jurado, A.M., Mora-Sotomayor, L., Caro, G.M., Lopez, S.N., Peinado-Gonzalez, V., Pla-Garcia, J., Manfredi, J.A.R., Romeral-Planello, J.J., Fuentes, S.A.S., Martinez, E.S., Redondo, J.T., Urqui-O'Callaghan, R., Mier, M.P.Z., Chipera, S., Lacour, J.L., Mouchien, P., Sirven, J.B., Manning, H., Fairén, A., Hayes, A., Joseph, J., Sullivan, R., Thomas, P., Dupont, A., Lundberg, A., Melikechi, N., Mezzacappa, A., DeMarines, J., Grinspoon, D., Reitz, G., Prats, B., Atlaskin, E., Genzer, M., Harri, A.M., Haukka, H., Kahanpaa, H., Kauhainen, J., Paton, M., Polkko, J., Schmidt, W., Siili, T., Fabre, C., Wray, J., Wilhelm, M.B., Poitrasson, F., Patel, K., Gorevan, S., Indyk, S., Paulsen, G., Bish, D., Gondet, B., Langevin, Y., Geffroy, C., Baratoux, D., Berger, G., Cros, A., d'Uston, C., Forni, O., Gasnault, O., Lasue, J., Lee, Q.M., Meslin, P.Y., Pallier, E., Parot, Y., Pinet, P., Schroder, S., Toplis, M., Lewin, E., Brunner, W., Heydari, E., Achilles, C., Sutter, B., Cabane, M., Coscia, D., Szopa, C., Robert, F., Sautter, V., Le Mouélic, S., Nachon, M., Buch, A., Stalport, F., Coll, P., Francois, P., Raulin, F., Teinturier, S., Cameron, J., Clegg, S., Cousin, A., DeLapp, D., Dingler, R., Jackson, R.S., Johnstone, S., Lanza, N., Little, C., Nelson, T., Williams, R.B., Jones, A., Kirkland, L., Baker, B., Cantor, B., Caplinger, M., Davis, S., Duston, B., Fay, D., Harker, D., Herrera, P., Jensen, E., Kennedy, M.R., Krezoski, G., Kryszak, D., Lipkaman, L., McCartney, E., McNair, S., Nixon, B., Posiolova, L., Ravine, M., Saloman, A., Saper, L., Stoiber, K., Supulver, K., Van Beek, J., Van Beek, T., Zimdar, R., French, K.L., Iagnemma, K., Miller, K., Goesmann, F., Goetz, W., Hviid, S., Johnson, M., Lefavor, M., Lyness, E., Breves, E., Dyar, M.D., Fassett, C., Edwards, L., Haberle, R., Hoehler, T., Hollingsworth, J., Kahre, M., Keely, L., McKay, C., Bleacher, L., Brinckerhoff, W., Choi, D., Dworkin, J. P., Floyd, M., Freissinet, C., Garvin, J., Glavin, D., Harpold, D., Martin, D.K., McAdam, A., Pavlov, A., Raaen, E., Smith, M.D., Stern, J., Tan, F., Trainer, M., Posner, A., Voytek, M., Aubrey, A., Behar, A., Blaney, D., Brinza, D., Christensen, L., DeFlores, L., Feldman, J., Feldman, S., Flesch, G., Jun, L., Keymeulen, D.,
- Mischna, M., Morookian, J.M., Pavri, B., Schoppers, M., Sengstacken, A., Simmonds, J.J., Spanovich, N., Juarez, M.D.L.T., Webster, C.R., Yen, A., Archer, P. D., Cucinotta, F., Jones, J.H., Morris, R.V., Niles, P., Rampe, E., Nolan, T., Fisk, M., Radziemski, L., Barraclough, B., Bender, S., Berman, D., Dobreá, E.N., Tokar, R., Cleghorn, T., Huntress, W., Manhes, G., Hudgins, J., Olson, T., Stewart, N., Sarrazin, P., Vicenzi, E., Bullock, M., Ehresmann, B., Hamilton, V., Hassler, D., Peterson, J., Rafkin, S., Zeitlin, C., Fedosov, F., Golovin, D., Karpushkina, N., Kozyrev, A., Litvak, M., Malakhov, A., Mitrofanov, I., Mokrousov, M., Nikiforov, S., Prokhorov, V., Sanin, A., Tretyakov, V., Varenikov, A., Vostrukhin, A., Kuzmin, R., Clark, B., Wolff, M., Botta, O., Drake, D., Bean, K., Lemmon, M., Schwenzner, S.P., Lee, E.M., Sucharski, R., Hernandez, M.A.D.P., Avalos, J.J.B., Ramos, M., Kim, M.H., Malespin, C., Plante, I., Muller, J.P., Navarro-Gonzalez, R., Ewing, R., Boynton, W., Downs, R., Fitzgibbon, M., Harshman, K., Morrison, S., Kortmann, O., Williams, A., Lugmair, G., Wilson, M.A., Jakosky, B., Balic-Zunic, T., Frydenvang, J., Jensen, J.K., Kinch, K., Koefoed, A., Madsen, M.B., Stipp, S.L.S., Boyd, N., Campbell, J.L., Perrett, G., Pradler, I., VanBommel, S., Jacob, S., Owen, T., Savijarvi, H., Boehm, E., Bottcher, S., Burmeister, S., Guo, J., Kohler, J., Garcia, C.M., Mueller-Mellin, R., Wimmer-Schweingruber, R., Bridges, J.C., McConochie, T., Benna, M., Franz, H., Bower, H., Brunner, A., Blau, H., Boucher, T., Carosino, M., Atreya, S., Elliott, H., Halleaux, D., Renno, N., Wong, M., Pepin, R., Elliott, B., Spray, J., Thompson, L., Gordon, S., Ollila, A., Williams, J., Vasconcelos, P., Bentz, J., Nealon, K., Popa, R., Moersch, J., Tate, C., Day, M., Francis, R., McCullough, E., Cloutis, E., Ten Kate, I.L., Scholes, D., Slavney, S., Stein, T., Ward, J., Berger, J., Moores, J.E., 2014. A habitable fluvio-lacustrine environment at Yellowknife Bay, Gale Crater, Mars. *Science* 343. <https://doi.org/10.1126/science.1242777>, 1242777–1242777.
- Hausrath, E., Ming, D., Peretyazhko, T., Rampe, E., 2018. Reactive transport and mass balance modeling of the Stimson sedimentary formation and altered fracture zones constrain diagenetic conditions at Gale crater, Mars. *Earth Planet. Sci. Lett.* 491, 1–10. URL: <https://linkinghub.elsevier.com/retrieve/pii/S0012821X18300992> <https://doi.org/10.1016/j.epsl.2018.02.037>.
- Hausrath, E.M., Ming, D.W., Rampe, E.B., Peretyazhko, T.S., 2021. Reactive transport modeling of aqueous alteration in the Murray formation, gale crater, mars. *ACS Earth Space Chem.* 5, 424–435.
- Hermanská, M., Voigt, M.J., Marieni, C., Declercq, J., Oelkers, E.H., 2022. A comprehensive and internally consistent mineral dissolution rate database: part I: primary silicate minerals and glasses. *Chem. Geol.* 597, 120807. URL: <https://linkinghub.elsevier.com/retrieve/pii/S0009254122001012> <https://doi.org/10.1016/j.chemgeo.2022.120807>.
- Hodson, M.E., 2006. Does reactive surface area depend on grain size? Results from ph 3, 25 c far-from-equilibrium flow-through dissolution experiments on anorthite and biotite. *Geochim. Cosmochim. Acta* 70, 1655–1667.
- Jensen, D.L., Boddum, J.K., Tjell, J.C., Christensen, T.H., 2002. The solubility of rhodochrosite (mnco₃) and siderite (feco₃) in anaerobic aquatic environments. *Appl. Geochem.* 17, 503–511.
- Jiang, C.Z., Tosca, N.J., 2020. Growth kinetics of siderite at 298.15 k and 1 bar. *Geochim. Cosmochim. Acta* 274, 97–117.
- Kan, C.C., Aganon, M.C., Futral, C.M., Dalida, M.L.P., 2013. Adsorption of mn²⁺ from aqueous solution using fe and mn oxide-coated sand. *J. Environ. Sci.* 25, 1483–1491.
- Koeppen, W.C., Hamilton, V.E., 2008. Global distribution, composition, and abundance of olivine on the surface of Mars from thermal infrared data. *J. Geophys. Res. Planets* 113.
- Konhauser, K.O., Planavsky, N., Hardisty, D., Robbins, L., Warchola, T., Haugaard, R., Lalonde, S., Partin, C., Oonk, P., Tsikos, H., et al., 2017. Iron formations: A global record of neoproterozoic to palaeoproterozoic environmental history. *Earth Sci. Rev.* 172, 140–177.
- Krasnopolsky, V.A., 2017. Annual mean mixing ratios of N₂, Ar, O₂, and CO in the martian atmosphere. *Planet. Space Sci.* 144, 71–73. URL: <https://linkinghub.elsevier.com/retrieve/pii/S003206317300545> <https://doi.org/10.1016/j.pss.2017.05.009>.
- Lan, S., Wang, X., Xiang, Q., Yin, H., Tan, W., Qiu, G., Liu, F., Zhang, J., Feng, X., 2017. Mechanisms of mn (ii) catalytic oxidation on ferrihydrate surfaces and the formation of manganese (oxyhydr) oxides. *Geochim. Cosmochim. Acta* 211, 79–96.
- Lanza, N.L., Wiens, R.C., Arvidson, R.E., Clark, B.C., Fischer, W.W., Gellert, R., Grotzinger, J.P., Hurowitz, J.A., McLennan, S.M., Morris, R.V., Atreya, S., Elliott, J.F., Berger, J.A., Blaney, D.L., Bridges, N.T., Calef, F., Campbell, J.L., Clegg, S.M., Cousin, A., Edgett, K.S., Fabre, C., Fisk, M.R., Forni, O., Frydenvang, J., Hardy, K.R., Hardgrove, C., Johnson, J.R., Lasue, J., Le Mouélic, S., Malin, M.C., Mangold, N., Martin-Torres, J., Maurice, S., McBride, M.J., Ming, D.W., Newsom, H.E., Ollila, A. M., Sautter, V., Schröder, S., Thompson, L.M., Treiman, A.H., VanBommel, S., Vaniman, D.T., Zorzano, M.P., 2016. Oxidation of manganese in an ancient aquifer, Kimberley formation, Gale crater, Mars: Manganese Fracture Fills in Gale Crater. *Geophys. Res. Lett.* 43, 7398–7407. URL: <http://doi.wiley.com/10.1002/2016GL069109> <https://doi.org/10.1002/2016GL069109>.
- Lasaga, A.C., 1981. Transition state theory. *Rev. Mineral.* 8.
- Lasaga, A.C., 1998. Kinetic Theory in the Earth Sciences. Princeton university press.
- Laxen, D.P., Davison, W., Woolf, C., 1984. Manganese chemistry in rivers and streams. *Geochim. Cosmochim. Acta* 48, 2107–2111.
- Lichter, P.C., 2016. Kinetic rate laws invariant to scaling the mineral formula unit. *Am. J. Sci.* 316, 437–469.
- Limmer, M.A., Linam, F.A., Evans, A.E., Seyfferth, A.L., 2023. Unraveling the mechanisms of fe oxidation and mn reduction on mn indicators of reduction in soil (iris) films. *Environ. Sci. Technol.* 57, 6530–6539.
- Loche, M., Fabre, S., Meslin, P.Y., Cousin, A., Lanza, N., Kah, L., Gasnault, O., Maurice, S., Wiens, R., 2022. Exploring the formation of the mn-p-fe-mg enrichment

- of the broken nodules in gale crater with source-to-sink geochemical modeling. In: Lunar and Planetary Science Conference, p. 1274.
- Loche, M., Fabre, S., Cousin, A., Treiman, A.A., Lanza, N., Meslin, P., Gasda, P., Das, D., Tutolo, B., Gasnault, O., et al., 2023. The fate of manganese: fractionation of mn and fe during the kinetic alteration process. In: Lunar and Planetary Science Conference, p. 2842.
- Mandon, L., Quantin-Nataf, C., Royer, C., Beck, P., Fouchet, T., Johnson, J., Dehouck, E., Le Mouélic, S., Poulet, F., Montmessin, F., et al., 2023. Reflectance of jezero crater floor: 2. Mineralogical interpretation. *J. Geophys. Res. Planets* 128, e2022JE007450.
- Mangold, N., Thompson, L.M., Forni, O., Williams, A.J., Fabre, C., Le Deit, L., Wiens, R. C., Williams, R., Anderson, R.B., Blaney, D.L., Calef, F., Cousin, A., Clegg, S.M., Dromart, G., Dietrich, W.E., Edgett, K.S., Fisk, M.R., Gasnault, O., Gellert, R., Grotzinger, J.P., Kah, L., Le Mouélic, S., McLennan, S.M., Maurice, S., Meslin, P.Y., Newsom, H.E., Palucis, M.C., Rapin, W., Sautter, V., Siebach, K.L., Stack, K., Sumner, D., Yingst, A., 2016. Composition of conglomerates analyzed by the Curiosity rover: Implications for Gale Crater crust and sediment sources: CONGLOMERATES COMPOSITION AT GALE CRATER. *J. Geophys. Res. Planets* 121, 353–387. URL: <http://doi.wiley.com/10.1002/2015JE004977> <https://doi.org/10.1002/2015JE004977>.
- Mangold, N., Dehouck, E., Fedo, C., Forni, O., Achilles, C., Bristow, T., Downs, R., Frydenvang, J., Gasnault, O., L'Haridon, J., et al., 2019. Chemical alteration of fine-grained sedimentary rocks at gale crater. *Icarus* 321, 619–631.
- Martin, S.T., 2005. Precipitation and dissolution of iron and manganese oxides. *Environ. Catal.* 1, 61–82.
- Marty, N.C., Claret, F., Lassina, A., Tremosa, J., Blanc, P., Madé, B., Giffaut, E., Cochebin, B., Tournassat, C., 2015. A database of dissolution and precipitation rates for clay-rocks minerals. *Appl. Geochem.* 55, 108–118. URL: <https://linkinghub.elsevier.com/retrieve/pii/S0883292714002443> <https://doi.org/10.1016/j.apgeochem.2014.10.012>.
- Meslin, P.Y., Gasda, P., L'Haridon, J., Forni, O., Lanza, N., Lamm, S., Johnson, J.R., Wiens, R.C., Thompson, L., Rapin, W., Gasnault, O., Cousin, A., Mangold, N., Dehouck, E., Maurice, S., Frydenvang, J., Lasue, J., 2018. Detection of hydrous manganese and iron oxides with variable phosphorus and magnesium contents in the lacustrine sediments of the Murray Formation, Gale, Mars. In: Lunar and Planetary Science Conference, p. 1447.
- Meunier, A., 2005. *Clays*. Springer Science & Business Media.
- Mills, J.V., Barnhart, H.A., DePaolo, D.J., Lammers, L.N., 2022. New insights into mn²⁺ and mg²⁺ inhibition of calcite growth. *Geochim. Cosmochim. Acta* 334, 338–367.
- Mitra, K., Moreland, E.L., Ledingham, G.J., Catalano, J.G., 2022. Formation of manganese oxides on early Mars due to active halogen cycling. *Nat. Geosci.* <https://doi.org/10.1038/s41561-022-01094-y>.
- Morgan, J.J., 2005. Kinetics of reaction between O₂ and Mn(II) species in aqueous solutions. *Geochim. Cosmochim. Acta* 69, 35–48. URL: <https://linkinghub.elsevier.com/retrieve/pii/S0016703704004533> <https://doi.org/10.1016/j.gca.2004.06.013>.
- Müller, M., Parkhurst, D.L., Charlton, S.R., 2011. Programming phreeqc calculations with c++ and python a comparative study. *Exchange* 1, 632–636.
- Myagkiy, A., Gouffier, F., Truche, L., Cathelineau, M., 2019. Reactive transport modeling applied to ni laterite ore deposits in New Caledonia: Role of hydrodynamic factors and geological structures in ni mineralization. *Geochem. Geophys. Geosyst.* 20, 1425–1440.
- Neugebauer, I., Thomas, C., Ordoñez, L., Waldmann, N.D., Recasens, C., Viczaino, A., Jimenez-Espejo, F.J., Ariztegui, D., 2022. Preservation of fe/mn-redox fronts in sediments of an oligotrophic, oxygenated deep-water lake (lago fagnano, Tierra del Fuego). *Sedimentology* 69, 1841–1860.
- Oelkers, E.H., Schott, J., Devidal, J.L., 1994. The effect of aluminum, ph, and chemical affinity on the rates of aluminosilicate dissolution reactions. *Geochim. Cosmochim. Acta* 58, 2011–2024.
- Oze, C., Sharma, M., 2007. Serpentinization and the inorganic synthesis of h₂ in planetary surfaces. *Icarus* 186, 557–561.
- Palandri, J.L., Kharaka, Y.K., 2004. A Compilation of Rate Parameters of Water-Mineral Interaction Kinetics for Application to Geochemical Modeling. Technical Report. Geological Survey, Menlo Park CA.
- Parkhurst, D.L., Appelo, C.A.J., 2013. Description of input and examples for PHREEQC version 3-A computer program for speciation, batch-reaction, one-dimensional transport, and inverse geochemical calculations. volume book 6 of Techniques and Methods. U.S. Geological Survey. URL: <https://pubs.usgs.gov/tm/06/a43/section/A43>.
- Rampe, Blake D., Bristow, T., Ming, D., Vaniman, D., Morris, R., Achilles, C., Chipera, S., Morrison, S., Tu, V., Yen, A., Castle, N., Downs, G., Downs, R., Grotzinger, J., Hazen, R., Treiman, A., Peretyazhko, T., Des Marais, D., Walroth, R., Craig, P., Crisp, J., Lafuente, B., Morookian, J., Sarrazin, P., Thorpe, M., Bridges, J., Edgar, L., Fedo, C., Freissinet, C., Gellert, R., Mahaffy, P., Newsom, H., Johnson, J., Kah, L., Siebach, K., Schieber, J., Sun, V., Vasavada, A., Wellington, D., Wiens, R., 2020a. Mineralogy and geochemistry of sedimentary rocks and eolian sediments in Gale crater, Mars: A review after six Earth years of exploration with Curiosity. *Geochemistry* 80, 125605. URL: <https://linkinghub.elsevier.com/retrieve/pii/S0009281920300064> <https://doi.org/10.1016/j.chemgeo.2020.125605>.
- Rampe, E., Blake, D., Bristow, T., Ming, D., Vaniman, D., Morris, R., Achilles, C., Chipera, S., Morrison, S., Tu, V., Yen, A., Castle, N., Downs, G., Downs, R., Grotzinger, J., Hazen, R., Treiman, A., Peretyazhko, T., Des Marais, D., Walroth, R., Craig, P., Crisp, J., Lafuente, B., Morookian, J., Sarrazin, P., Thorpe, M., Bridges, J., Edgar, L., Fedo, C., Freissinet, C., Gellert, R., Mahaffy, P., Newsom, H., Johnson, J., Kah, L., Siebach, K., Schieber, J., Sun, V., Vasavada, A., Wellington, D., Wiens, R., 2020b. Mineralogy and geochemistry of sedimentary rocks and eolian sediments in Gale crater, Mars: A review after six Earth years of exploration with Curiosity. *Geochemistry* 80, 125605. URL: <https://linkinghub.elsevier.com/retrieve/pii/S0009281920300064> <https://doi.org/10.1016/j.chemgeo.2020.125605>.
- Rapin, W., Ehlmann, B.L., Dromart, G., Schieber, J., Thomas, N.H., Fischer, W.W., Fox, V. K., Stein, N.T., Nachon, M., Clark, B.C., Kah, L.C., Thompson, L., Meyer, H.A., Gabriel, T.S.J., Hardgrove, C., Mangold, N., Rivera-Hernandez, F., Wiens, R.C., Vasavada, A.R., 2019. An interval of high salinity in ancient Gale crater lake on Mars. *Nat. Geosci.* 12, 889–895. URL: <http://www.nature.com/articles/s41561-019-0458-8> <https://doi.org/10.1038/s41561-019-0458-8>.
- Rivera-Hernández, F., Sumner, D.Y., Mangold, N., Banham, S.G., Edgett, K.S., Fedo, C.M., Gupta, S., Gwizd, S., Heydari, E., Maurice, S., et al., 2020. Grain size variations in the Murray formation: Stratigraphic evidence for changing depositional environments in gale crater, mars. *J. Geophys. Res. Planets* 125, e2019JE006230.
- Roscoe, S., 1973. The huronian supergroup, a paleoarchean succession showing evidence of atmospheric evolution. *Geol. Assoc. Can. Spec. Pap.* 12, 31–47.
- Sengupta, R., Tosca, N.J., Robinson, S.A., 2020. Geochemical controls on the elemental composition of siderite: Implications for palaeo-environmental reconstructions. *Geochim. Cosmochim. Acta* 271, 1–15.
- Siever, R., Woodford, N., 1979. Dissolution kinetics and the weathering of mafic minerals. *Geochim. Cosmochim. Acta* 43, 717–724.
- Sigg, L., Behra, P., Stumm, W., 2022. *Chimie des milieux aquatiques-5e éd.* Dunod.
- Singer, P.C., Stumm, W., 1970. Acidic Mine Drainage: The Rate-Determining Step. Science (American Association for the Advancement of Science), 167. United States Publisher: American Association for the Advancement of Science, Place, pp. 1121–1123.
- Sowiński, P., 2016. Effect of slope position on soil particle-size distribution in young glacial landscape (lyna river valley, ne Poland). *Soil Sci. Annu.* 67.
- Steefel, C.I., 2019. Reactive transport at the crossroads. *Rev. Mineral. Geochem.* 85, 1–26.
- Steefel, C.I., DePaolo, D.J., Lichtner, P.C., 2005. Reactive transport modeling: an essential tool and a new research approach for the earth sciences. *Earth Planet. Sci. Lett.* 240, 539–558.
- Stopar, J.D., Jeffrey Taylor, G., Hamilton, V.E., Browning, L., 2006. Kinetic model of olivine dissolution and extent of aqueous alteration on mars. *Geochim. Cosmochim. Acta* 70, 6136–6152. URL: <https://linkinghub.elsevier.com/retrieve/pii/S0016703706020102> <https://doi.org/10.1016/j.gca.2006.07.039>.
- Tabata, H., 2021. An experimental study of photo-oxidation of Fe(II): Implications for the formation of Fe(III) (hydro)oxides on early Mars and Earth. *Geochim. Cosmochim. Acta* 17.
- Tester, J.W., Worley, W.G., Robinson, B.A., Grigsby, C.O., Feerer, J.L., 1994. Correlating quartz dissolution kinetics in pure water from 25 to 625 c. *Geochim. Cosmochim. Acta* 58, 2407–2420.
- Tice, M.M., Hurovitz, J.A., Allwood, A.C., Jones, M.W., Orenstein, B.J., Davidoff, S., Wright, A.P., Pedersen, D.A., Henneke, J., Tosca, N.J., et al., 2022. Alteration history of sêitah formation rocks inferred by pixl x-ray fluorescence, x-ray diffraction, and multispectral imaging on mars. *Sci. Adv.* 8, eabp9084.
- Tosca, N.J., Knoll, A.H., 2009. Juvenile chemical sediments and the long term persistence of water at the surface of mars. *Earth Planet. Sci. Lett.* 286, 379–386.
- Tosca, N.J., Tutolo, B.M., 2023. How to make an alkaline lake: fifty years of chemical divides. *Elements* 19, 15–21.
- Tosca, N.J., Ahmed, I.A., Tutolo, B.M., Ashpittel, A., Hurovitz, J.A., 2018. Magnetite authigenesis and the warming of early mars. *Nat. Geosci.* 11, 635–639.
- Treiman, A.H., Downs, R.T., Ming, D.W., Morris, R.V., Thorpe, M.T., Hazen, R.M., Downs, G.W., Rampe, E.B., CheMin Team, T., 2021. Possible detection of a Jahnsite-Whiteite Group phosphate mineral by MSL CheMin in Glen Torridon, Gale Crater, Mars. In: Lunar and Planetary Science Conference, p. 1200.
- Treiman, A.H., Lanza, N.L., VanBommel, S., Berger, J., Wiens, R., Bristow, T., Johnson, J., Rice, M., Hart, R., McAdam, A., et al., 2023. Manganese-iron phosphate nodules at the gale crater, mars. *Minerals* 13, 1122.
- Turbet, M., Forget, F., 2021. 3-D Global modelling of the early martian climate under a dense CO₂+H₂ atmosphere and for a wide range of surface water inventories. URL: <http://arxiv.org/abs/2103.10301> arXiv:2103.10301 [astro-ph, physics: physics].
- Tutolo, B., Haurath, E., Rampe, E., Bristow, T., Downs, R., Kite, E., Pere, T., Thorpe, M., Grotzinger, J., Archer, D., Des Marais, D., Blake, D., Vaniman, D., Morrison, S., Chipera, S., Hazen, R., Morris, R., Tu, V., Simpson, S., Pandey, A., Yen, A., Treiman, A., Larter, S., Craig, P., Castle, N., Ming, D., Meusburger, J., Gasda, P., Frydenvang, J., 2024. In situ evidence for an active carbon cycle on ancient mars. In: Lunar and Planetary Science Conference, p. 1564.
- Vaniman, D.T., Martínez, G.M., Rampe, E.B., Bristow, T.F., Blake, D.F., Yen, A.S., Ming, D.W., Rapin, W., Meslin, P.Y., Morookian, J.M., Downs, R.T., Chipera, S.J., Morris, R.V., Morrison, S.M., Treiman, A.H., Achilles, C.N., Robertson, K., Grotzinger, J.P., Hazen, R.M., Wiens, R.C., Sumner, D.Y., 2018. Gypsum, bassanite, and anhydrite at Gale crater, Mars. *Am. Mineral.* 103, 1011–1020. URL: <https://www.degruyter.com/document/doi/10.2138/am-2018-6346/html> <https://doi.org/10.2138/am-2018-6346>.
- Viennet, J.C., Bultel, B., Werner, S.C., 2019. Experimental reproduction of the martian weathering profiles argues for a dense Noachian CO₂ atmosphere. *Chem. Geol.* 525, 82–95. URL: <https://linkinghub.elsevier.com/retrieve/pii/S0009254119303298> <https://doi.org/10.1016/j.chemgeo.2019.07.009>.

- Wiens, R.C., Udry, A., Beyssac, O., Quantin-Nataf, C., Mangold, N., Cousin, A., Mandon, L., Bosak, T., Forni, O., McLennan, S.M., Sautter, V., Brown, A., Benzerara, K., Johnson, J.R., Mayhew, L., Maurice, S., Anderson, R.B., Clegg, S.M., Crumpler, L., Gabriel, T.S.J., Gasda, P., Hall, J., Horgan, B.H.N., Kah, L., Legett, C., Madariaga, J.M., Meslin, P.Y., Ollila, A.M., Poulet, F., Royer, C., Sharma, S.K., Siljeström, S., Simon, J.I., Acosta-Maeda, T.E., Alvarez-Llamas, C., Angel, S.M., Arana, G., Beck, P., Bernard, S., Bertrand, T., Bousquet, B., Castro, K., Chide, B., Clavé, E., Cloutis, E., Connell, S., Dehouck, E., Dromart, G., Fischer, W., Fouchet, T., Francis, R., Frydenvang, J., Gasnault, O., Gibbons, E., Gupta, S., Hausrath, E.M., Jacob, X., Kalucha, H., Kelly, E., Knutsen, E., Lanza, N., Laserna, J., Lasue, J., Le Mouélic, S., Leveille, R., Lopez Reyes, G., Lorenz, R., Manrique, J.A., Martínez-Frias, J., McConnochie, T., Melikechi, N., Mimoun, D., Montmessin, F., Moros, J., Murdoch, N., Pilleri, P., Pilorget, C., Pinet, P., Rapin, W., Rull, F., Schröder, S., Shuster, D.L., Smith, R.J., Stott, A.E., Tarnas, J., Turenne, N., Veneranda, M., Vogt, D.S., Weiss, B.P., Willis, P., Stack, K.M., Williford, K.H., Farley, K.A., The SuperCam Team, 2022. Compositionally and density stratified igneous terrain in Jezero crater, Mars. *Sci. Adv.* 8, eabo3399. URL: <https://www.science.org/doi/10.1126/sciadv.abo3399> <https://doi.org/10.1126/sciadv.abo3399>
- Wordsworth, R., Kalugina, Y., Lokshtanov, S., Viganin, A., Ehlmann, B., Head, J., Sanders, C., Wang, H., 2017. Transient reducing greenhouse warming on early Mars. *Geophys. Res. Lett.* 44, 665–671. URL: <https://onlinelibrary.wiley.com/doi/abs/10.1002/2016GL071766> <https://doi.org/10.1002/2016GL071766>
- Wordsworth, R., Knoll, A.H., Hurowitz, J., Baum, M., Ehlmann, B.L., Head, J.W., Steakley, K., 2021. A coupled model of episodic warming, oxidation and geochemical transitions on early Mars. *Nat. Geosci.* 14, 127–132. URL: <http://arxiv.org/abs/2103.06736> <https://doi.org/10.1038/s41561-021-00701-8>. arXiv: 2103.06736.
- Yeghicheyan, D., Aubert, D., Bouhnik-le Coz, M., Chmeleff, J., Delpoux, S., Djouaraev, I., Granier, G., Lacan, F., Piro, J.L., Rousseau, T., et al., 2019. A new interlaboratory characterisation of silicon, rare earth elements and twenty-two other trace element concentrations in the natural river water certified reference material slrs-6 (nrc-cnrc). *Geostand. Geoanal. Res.* 43, 475–496.
- Yeghicheyan, D., Grinberg, P., Alleman, L.Y., Belhadj, M., Causse, L., Chmeleff, J., Cordier, L., Djouaraev, I., Dumoulin, D., Dumont, J., et al., 2021. Collaborative determination of trace element mass fractions and isotope ratios in aqua-1 drinking water certified reference material. *Anal. Bioanal. Chem.* 413, 4959–4978.
- Zhu, C., Lu, P., 2013. The coupling of dissolution and precipitation reactions as the main contributor to the apparent field-lab rate discrepancy. *Proc. Earth Planet. Sci.* 7, 948–952.
- Zolotov, M.Y., Mironenko, M.V., 2007. Timing of acid weathering on Mars: A kinetic-thermodynamic assessment. *J. Geophys. Res.* 112, E07006. URL: <http://doi.wiley.com/10.1029/2006JE002882> <https://doi.org/10.1029/2006JE002882>